

Radius-Flow Entanglement in Hadron States and Gravitational Form Factors

Kiminad A. Mamo¹

¹*Department of Physics, University of Connecticut, Storrs, CT 06269-3046, USA**

(Dated: March 5, 2026)

We propose a lattice-ready entanglement observable for QCD hadrons: the vacuum-subtracted radius flow of the ball Rényi entropy, $\mathfrak{s}_n(R; h) \equiv R \partial_R \Delta S_n(B_R; h)$, defined via the Euclidean replica cut-and-glue construction in a rest-frame momentum-projected one-hadron state, with spin averaging performed at the level of the final flow. In the continuum, varying R at fixed shape is equivalent to a Weyl rescaling, so the flow is trace selected and admits a surface-plus-remainder organization on the entangling sphere. We use this to formulate a lattice stability test of boundary dominance: fit the measured flow on local R windows to a low-curvature remainder plus a small template basis built from hadronic gravitational form factors (GFFs). The two endpoint templates are the spin-0/trace shape $\mathfrak{t}_h^{(0)}(R) = R^3 \rho_S(R)$ constructed from $A^S(t)$ and a spin-2/TT proxy $\mathfrak{t}_h^{(2)}(R) = R^3 \rho_A(R)$ constructed from $A(t)$, together with the mixed family $\mathfrak{t}_h^{\text{mix}}(R; c_0, c_2) = c_0 \mathfrak{t}_h^{(0)}(R) + c_2 \mathfrak{t}_h^{(2)}(R)$. A soft-wall AdS/QCD appendix shows that the pole-subtracted integrated trace-energy correlator closes on this same $\{A^S, A\}$ basis and supplies a model-dependent benchmark ratio for c_0/c_2 ; for lattice comparison the coefficients are left free and extracted from data. For representative nucleon dipole inputs, the pure endpoints predict distinct single-extremum scales, $R_{\text{EE}}^{(0)} \sim 0.84$ fm and $R_{\text{EE}}^{(2)} \sim 0.43$ fm, enabling discrimination among scalar control, spin-2 control, and genuine mixing through the turning-point location, the sign change of the slope across it, and the fitted ratio of template weights.

I. INTRODUCTION

Spatial entanglement probes correlations across an entangling surface and is intrinsically nonlocal [1–16]. In continuum QFT, entanglement entropies are UV dominated by short-distance modes near the cut, so UV-finite, state-dependent information is most cleanly accessed through vacuum subtraction and size derivatives that remove state-independent geometric contributions [4, 17, 18]. For QCD this motivates a direct lattice diagnostic: define a gauge-invariant subsystem observable in a one-hadron state, scan it with the subsystem size, and test whether it exhibits hadronic-scale structure. The purpose of this paper is operational. We define a lattice-ready observable, formulate a stability-based boundary-dominance test, and compare the resulting hypothesis space to hadronic gravitational form factors (GFFs).

We work with the Euclidean replica cut-and-glue definition of reduced density matrices in gauge theory. Choose a spatial ball B_R at Euclidean time $\tau = 0$ and define ρ_{B_R} by gluing the complement across the cut and leaving independent boundary data on B_R , as in the standard Buividovich-Polikarpov prescription and its successors [18–25]¹. On the lattice one evaluates $\text{Tr}(\rho_{B_R}^n)$ as a ratio of partition functions on an n -sheeted cut geometry, so the primary practical focus is small integer Rényi index $n \geq 2$, especially $n = 2$.

The hadron state is prepared in the usual way by momentum projection on a finite periodic volume. We spe-

cialize to a rest-frame one-hadron state with definite spin projection, $\rho_{h,\lambda} = |h(\mathbf{0}), \lambda\rangle \langle h(\mathbf{0}), \lambda|$. For integer $n \geq 2$ we define the vacuum-subtracted Rényi entropy

$$\Delta S_n(B_R; h, \lambda) \equiv S_n(B_R; \rho_{h,\lambda}) - S_n(B_R; \rho_0), \quad (1)$$

and its logarithmic size derivative (the radius flow)

$$\mathfrak{s}_n(R; h, \lambda) \equiv R \frac{d}{dR} \Delta S_n(B_R; h, \lambda). \quad (2)$$

The von Neumann limit $n \rightarrow 1$ is used only as a notational convenience when writing continuum response identities: $\Delta S_{\text{EE}}(B_R; h, \lambda) = S_{\text{EE}}(B_R; \rho_{h,\lambda}) - S_{\text{EE}}(B_R; \rho_0)$ and $\mathfrak{s}_{\text{EE}}(R; h, \lambda) = R d \Delta S_{\text{EE}} / dR$.

For lattice applications one typically reports unpolarized results. For entanglement it is important to distinguish averaging *final observables* over polarizations from taking the entropy of an incoherent spin mixture. We adopt the former: unpolarized results are obtained by averaging the *flow* over λ ,

$$\mathfrak{s}_n(R; h) \equiv \frac{1}{2S+1} \sum_{\lambda=-S}^S \mathfrak{s}_n(R; h, \lambda), \quad (3)$$

(and analogously for \mathfrak{s}_{EE}), which avoids a spurious large- R constant shift associated with mixed-state entropies.

A rest-frame momentum eigenstate on a periodic lattice is spatially delocalized, so one does not take a controlled $R \rightarrow \infty$ limit at fixed state. In practice one works in the window $a \ll R \ll L/2$ (lattice spacing a , spatial box size L), where the ball is well resolved and finite-volume wrap-around effects are parametrically suppressed. The key point is that the radius flow is not meant to be interpreted as a probability distribution in R

* ska25005@uconn.edu

¹ Other gauge-theory computations of entanglement entropy include [26–32].

or as a localization diagnostic for a hadron center of mass. Rather, it is a response observable defined by the replica geometry and operator insertions; any universal “which-side” occupancy background associated with delocalization varies smoothly with R in the working window and can be treated as part of the low-curvature remainder sector (App. H). In particular, a pure occupancy model cannot generate a narrow hadronic-scale extremum in $a \ll R \ll L/2$.

The continuum organizing principle is that a size change at fixed shape can be represented (after an appropriate diffeomorphism that holds the cut locus fixed in coordinates) as a Weyl rescaling of the background metric. A Weyl response couples to the trace $T \equiv T^\mu{}_\mu$, so the radius flow is trace selected. At leading order it admits a modular-correlator (source-detector) representation of the schematic form $\sim \int \sqrt{g} \langle T^\mu{}_\mu(x) K(R) \rangle$ (Sec. IV), where $K(R) = -\ln \rho_{B_R}$ is the modular Hamiltonian. This makes clear that the flow is an integrated response functional rather than a probability density, and that the Breit-frame profiles introduced below are used only as response templates for the R dependence, with no probabilistic interpretation assumed for the corresponding Breit densities [33, 34]. The comparison to Breit-frame profiles is therefore purely functional: one matches the measured R dependence of an extracted boundary contribution to a small template basis.

A quantitative identification of fitted coefficients with continuum-normalized EMT matrix elements requires an explicit lattice EMT/trace renormalization and matching procedure; here we deliberately formulate the comparison at the level of R -dependence (shape), absorbing normalization into fit coefficients and packaging residual contact-term structure into the remainder sector.

After vacuum subtraction and trace-channel renormalization within a fixed replica/cut prescription, the τ -integrated trace response admits a surface-supported distributional organization on the entangling sphere $\Sigma = \partial B_R$ plus a regular remainder (Sec. V). The basic mechanism is simple: the radius derivative probes the non-smoothness of the ball test function at $r = R$, and short-distance singularities in stress-tensor correlators reorganize into terms supported on Σ when integrated against that test function (see App. D for the distributional/OPE bookkeeping). This motivates decompositions of the form

$$\mathfrak{s}_n(R; h) = c_{\Sigma, n}(R; h) + \mathfrak{s}_n^{\text{reg}}(R; h), \quad (4)$$

where $c_{\Sigma, n}$ isolates the leading ($k = 0$) surface distribution and $\mathfrak{s}_n^{\text{reg}}$ packages higher-derivative surface terms together with bulk-regular contributions. We do not attempt to isolate $c_{\Sigma, n}$ directly on the lattice. Instead, we fit the full measured flow $\mathfrak{s}_n^{\text{lat}}(R)$ to (templates + a low-curvature remainder) on local R windows, and interpret stable template dominance as evidence that $c_{\Sigma, n}(R; h)$ controls the leading nontrivial R dependence on that window; the explicit curvature diagnostics are introduced with the fitting protocol in Sec. V. In practice $\mathfrak{s}_n(R)$ is

obtained from correlated fits to $\Delta S_n(R)$ or correlated finite differences, since pointwise differencing amplifies the noise and correlations.

Assuming such a window exists, the main physics question is which element of the spin-0/spin-2 GFF basis controls the leading boundary term. Trace selection constrains the operator channel in the continuum response, but the leading boundary coefficient extracted after renormalization and surface isolation is dynamical. In particular, the soft-wall holographic QCD computation in App. L shows that even for a trace-energy correlator the surviving nonlocal piece closes on the two-function basis $\{A^S(t), A(t)\}$, motivating a two-template hypothesis space rather than a single trace template. Trace selection therefore makes the scalar template $\mathfrak{t}_h^{(0)}(R) = R^3 \rho_S(R)$ built from $A^S(t)$ the natural baseline, but it does not by itself exclude competing boundary control by the $A(t)$ channel. Trace selection constrains the source operator channel, but not the spectral decomposition of the nonlocal boundary coefficient after pole subtraction and contact-term removal; in the soft-wall model that coefficient projects onto $\{A^S, A\}$ rather than $\{A^S\}$ alone.

We therefore treat the lattice comparison as a small hypothesis space with two pure endpoints,

$$\mathfrak{t}_h^{(0)}(R) = R^3 \rho_S(R), \quad \mathfrak{t}_h^{(2)}(R) = R^3 \rho_A(R),$$

where the factor R^3 is included simply to form a dimensionless radial template in three spatial dimensions (any overall normalization is absorbed into fitted coefficients), and the mixed family

$$\mathfrak{t}_h^{\text{mix}}(R; c_0, c_2) = c_0 \mathfrak{t}_h^{(0)}(R) + c_2 \mathfrak{t}_h^{(2)}(R), \quad (5)$$

equivalently associated in momentum space with

$$G_{\text{mix}}(t; c_0, c_2) = c_0 A^S(t) + c_2 A(t). \quad (6)$$

The pure scalar and pure spin-2 limits are recovered by $c_2 = 0$ and $c_0 = 0$, respectively.

A useful clue comes from the pole-subtracted integrated trace-energy correlator in soft-wall AdS/QCD. As shown in App. L, after elastic pole subtraction and the exact integrated projection $q_1 = 0$ the s - and u -channel exchange graphs drop out, while the remaining t -channel TT and spin-0 exchanges factorize onto $A(t)$ and $A^S(t)$. The resulting momentum-space hadron central charge is controlled by

$$\mathfrak{c}_{h, i}(t; E_h, M_h) \propto \left[\left(1 - \frac{1}{3} \frac{M_h^2}{E_h^2} \right) A_i(t) - \frac{9}{32} \frac{M_h^2}{E_h^2} A_i^S(t) \right], \quad (7)$$

with $E_h = \sqrt{M_h^2 + \vec{p}^2}$, and reduces at large E_h/M_h to

$$\mathfrak{c}_{h, i}(t; E_h \rightarrow \infty, M_h) \propto A_i(t), \quad (8)$$

Thus the leading large-energy response is governed by $A_i(t)$, while the scalar/trace piece is suppressed by M_h^2/E_h^2 . This is an IMF/large-energy statement, not an

exact finite-energy identity. The soft-wall derivation itself is for a scalar target and is used here only to motivate the $\{A^S, A\}$ basis and a benchmark ratio within that basis.

Existing lattice entanglement studies in non-Abelian gauge theory have largely focused on the vacuum (e.g. slab/strip geometries and UV-finite size derivatives such as the entropic C -function) [18, 22–25], and complementary work has investigated entanglement in the presence of external static color sources and confining flux tubes [35–40]. These programs establish important benchmarks and methodology. The physically complementary target—still largely unexplored—is state-dependent entanglement in a one-hadron state prepared by standard momentum projection. This observable directly probes how gauge-invariant correlations are reorganized in the singlet sector by the hadron, and it is accessible with existing lattice technology: the replica cut geometry used for S_n combined with conventional hadron source–sink preparation on each replica sheet.

A minimal first measurement is $\mathfrak{s}_2(R)$ for a nucleon (or pion) in the rest frame, scanned over $a \ll R \ll L/2$ with standard center/rotation averaging to control cut discretization. The stability tests must be repeated under reasonable variations of the ball boundary discretization (center shifts, cubic rotations, and alternative boundary implementations) to assess cut systematics. The immediate outputs are whether a pronounced intermediate- R extremum exists, whether the slope changes sign across it, and whether the data prefer a pure or genuinely mixed GFF description. For context, Ref. [41] analyzed a closely related boundary-localization criterion in the infinite-momentum frame, where transverse densities admit a partonic impact-parameter interpretation; we reserve the term *entropic confinement* for that IMF reading. Here we instead target a rest-frame, lattice-implementable observable: a momentum-projected hadron state on a Euclidean replica manifold, with Breit-frame (equal-time, 3D) GFF profiles used only as response templates for the R dependence, not as probability densities.

Throughout, ΔS_n and \mathfrak{s}_n are exact lattice observables at fixed replica/cut prescription, whereas boundary dominance, successful GFF matching, and agreement with the holographic benchmark are empirical questions. Our paper is organized as follows. Section II reviews cut-and-glue reduced density matrices and the rest-frame state preparation on the replicated manifold. Section III defines ball Rényi entropies, vacuum subtraction, and the radius-flow observable. Section IV develops the continuum response organizing principle and the trace-selected modular-correlator form. Section V gives the surface-supported organization of the renormalized trace response and formulates the boundary-dominance stability protocol. Section VI defines the pure spin-0 and spin-2 endpoint templates, the mixed template family, and the holographic benchmark subfamily. Section VII states the main lattice-facing hypotheses, the mixed-basis fitting strategy, and the falsifiers. Appendices collect technical

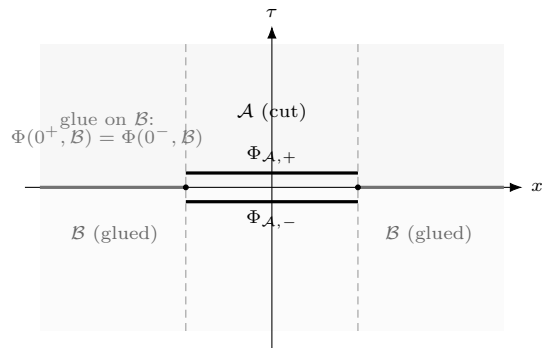


FIG. 1. **Cut-and-glue definition of the reduced density matrix kernel.** At the Euclidean time cut $\tau = 0$, the complement \mathcal{B} is glued by imposing $\Phi(0^+, \mathcal{B}) = \Phi(0^-, \mathcal{B})$ and integrating over $\Phi_{\mathcal{B}}$, while the region \mathcal{A} is left open so that independent boundary data $\Phi_{\mathcal{A},+}$ and $\Phi_{\mathcal{A},-}$ live on the two sides of the cut. The resulting path integral defines $\rho_{\mathcal{A}}[\Phi_{\mathcal{A},+}, \Phi_{\mathcal{A},-}]$ and is the basic building block for the replica construction of $\text{Tr}(\rho_{\mathcal{A}}^n)$ illustrated in Fig. 3.

details, including an occupancy toy model (App. H), optional wave-packet imaging formulas for local operators (App. I), lattice implementation notes (App. K), and the holographic central-charge argument (App. L).

II. EUCLIDEAN REDUCED DENSITY MATRICES IN QCD: CUT-AND-GLUE AND LATTICE READINESS

We work in Euclidean signature with fields Φ (gauge, quark, and if gauge fixed also ghosts) and Euclidean action $S_E[\Phi; g]$, with all couplings and renormalization parameters left implicit. Choose a cut at Euclidean time $\tau = 0$ and a spatial region $\mathcal{A} \subset \Sigma_{\text{tot}}$ with complement $\mathcal{B} = \Sigma_{\text{tot}} \setminus \mathcal{A}$ and entangling surface $\Sigma = \partial\mathcal{A}$.

A. Vacuum reduced density matrix kernel

Let $\Phi_{\pm}(\mathbf{x})$ denote boundary field configurations on $\tau = 0^{\pm}$, split as $\Phi_{\pm} = (\Phi_{\mathcal{A},\pm}, \Phi_{\mathcal{B},\pm})$. The vacuum reduced density matrix kernel on \mathcal{A} is [42–45]

$$\rho_{\mathcal{A},0}[\Phi_{\mathcal{A},+}, \Phi_{\mathcal{A},-}] = \frac{1}{\mathcal{N}_0} \int \mathcal{D}\Phi e^{-S_E[\Phi;g]} \Bigg|_{\substack{\Phi(0^+, \mathcal{A}) = \Phi_{\mathcal{A},+} \\ \Phi(0^-, \mathcal{A}) = \Phi_{\mathcal{A},-} \\ \Phi(0^+, \mathcal{B}) = \Phi(0^-, \mathcal{B})}} \quad (9)$$

Tracing out \mathcal{B} is implemented by gluing across the cut on \mathcal{B} while leaving \mathcal{A} open, see Fig. 1.

B. Rest-frame hadron preparation in Euclidean time

On a finite periodic lattice, a definite-momentum hadron state is prepared by standard momentum projec-

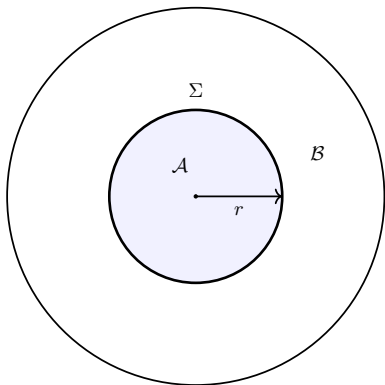


FIG. 2. Spherical region $\mathcal{A} = B_R$ bounded by the entangling surface $\Sigma = \partial\mathcal{A}$ (inner circle is a 1D illustration of the 2D surface).

tion. We focus on the rest frame $\mathbf{p}_0 = \mathbf{0}$. Let $\mathcal{O}_H(\tau, \mathbf{x})$ be a hadron interpolating operator with the appropriate quantum numbers and a fixed spin projection λ imposed by the usual Dirac/projector choices at source and sink. Define the momentum-projected interpolator

$$\mathcal{O}_H(\tau; \mathbf{p}_0) \equiv \int d^3\mathbf{x} e^{-i\mathbf{p}_0 \cdot \mathbf{x}} \mathcal{O}_H(\tau, \mathbf{x}), \quad \mathbf{p}_0 = \mathbf{0}, \quad (10)$$

so $\mathcal{O}_H(\tau; \mathbf{0}) = \int d^3\mathbf{x} \mathcal{O}_H(\tau, \mathbf{x})$.

Define Euclidean source/sink functionals at $\tau_i < 0 < \tau_f$,

$$\mathcal{S}_0^\dagger[\Phi] \equiv \mathcal{O}_H^\dagger(\tau_i; \mathbf{0}), \quad \mathcal{S}_0[\Phi] \equiv \mathcal{O}_H(\tau_f; \mathbf{0}). \quad (11)$$

Then the global cut density matrix kernel for the hadronic pure rest-frame state is

$$\rho_{h,\lambda}[\Phi_+, \Phi_-] = \frac{1}{\mathcal{N}_h} \int \mathcal{D}\Phi e^{-S_E[\Phi; g]} \mathcal{S}_0[\Phi] \mathcal{S}_0^\dagger[\Phi] \Big|_{\substack{\Phi(0^-) = \Phi_- \\ \Phi(0^+) = \Phi_+}}. \quad (12)$$

The reduced density matrix on \mathcal{A} is obtained by the same gluing on \mathcal{B} :

$$\rho_{\mathcal{A},h,\lambda}[\Phi_{\mathcal{A},+}, \Phi_{\mathcal{A},-}] = \int \mathcal{D}\Phi_{\mathcal{B}} \rho_{h,\lambda}[(\Phi_{\mathcal{A},+}, \Phi_{\mathcal{B}}), (\Phi_{\mathcal{A},-}, \Phi_{\mathcal{B}})]. \quad (13)$$

For Rényi entropies at integer $n \geq 2$, the same rest-frame source/sink functional that prepares $|h(\mathbf{0}), \lambda\rangle$ is inserted on *each* replica sheet of the n -sheeted manifold \mathcal{M}_n , see Fig. 3. Equivalently, one evaluates $Z_n[h]$ on \mathcal{M}_n with n identical rest-frame source-sink insertions and forms the standard ratio $Z_n[h]/(Z_1[h])^n$ (and its vacuum counterpart for subtraction) before taking the logarithmic combination defining S_n . This is directly analogous to standard multipoint correlators; the only new ingredient is the replicated cut geometry.

III. BALL RÉNYI ENTROPIES AND THE RADIUS-FLOW OBSERVABLE

We specialize to a spherical region,

$$\mathcal{A} \equiv B_R = \{\mathbf{x} \in \mathbb{R}^3 : r \equiv |\mathbf{x}| < R\}, \quad \Sigma \equiv \partial B_R = \{r = R\}. \quad (14)$$

For any state ρ and integer $n \geq 2$, the Rényi entropies are

$$S_n(B_R; \rho) \equiv \frac{1}{1-n} \ln \text{Tr}_{B_R}(\rho_{B_R}^n), \quad \rho_{B_R} \equiv \text{Tr}_{\mathcal{B}} \rho. \quad (15)$$

The von Neumann entropy is recovered by analytic continuation,

$$S_{\text{EE}}(B_R; \rho) \equiv -\text{Tr}_{B_R}(\rho_{B_R} \ln \rho_{B_R}) = \lim_{n \rightarrow 1} S_n(B_R; \rho), \quad (16)$$

and defines the modular Hamiltonian $K_\rho(R) \equiv -\ln \rho_{B_R}$.

In 3+1 dimensions the raw entanglement entropies contain geometric UV divergences. For a fixed replica/cut prescription, the UV structure in an arbitrarily small neighborhood of Σ is state independent, so divergent and Σ -localized UV pieces cancel in the vacuum subtraction Eq. (1) (and likewise in the $n \rightarrow 1$ limit).

The primary lattice-facing observable is the radius flow Eq. (2). It is insensitive to R -independent additive constants in ΔS_n and is directly measured as a function of R at fixed state preparation. Once $\mathfrak{s}_n(R; h, \lambda)$ is known, $\Delta S_n(B_R; h, \lambda)$ is obtained by integrating the flow,

$$\Delta S_n(B_R; h, \lambda) = \int^R \frac{dR'}{R'} \mathfrak{s}_n(R'; h, \lambda) + \text{constant}, \quad (17)$$

where the constant is fixed by a convention.

IV. ENTANGLEMENT RESPONSE: THE RADIUS FLOW AS AN INTEGRATED TRACE-CHANNEL MODULAR CORRELATOR

We use $x = (\tau, \mathbf{x})$ for spacetime points and bold symbols for spatial vectors. Unless stated otherwise we work in $d = 4$ spacetime dimensions. The lattice observable is $\mathfrak{s}_n(R)$ at small integer n . We present the response density and Rosenhaus-Smolkin correlator form in the $n \rightarrow 1$ limit for notational economy; the same Weyl/trace-selection logic is implemented on the replica manifold \mathcal{M}_n at integer n .

A. Metric response and the Weyl-flow identity

Following Refs. [12, 13], define the entanglement response density

$$\mathcal{T}_{\mu\nu}^{\text{EE}}(x | B_R; \rho) \equiv \frac{1}{\sqrt{g(x)}} \frac{\delta S_{\text{EE}}(B_R; \rho)}{\delta g^{\mu\nu}(x)}, \quad (18)$$

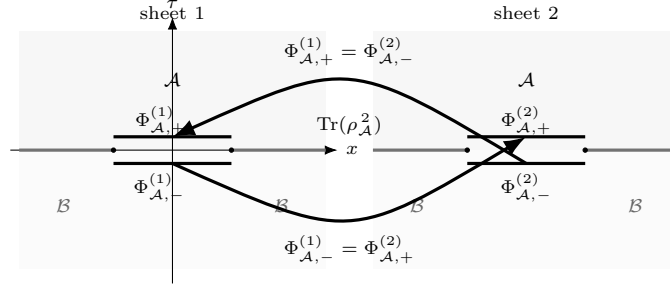


FIG. 3. **Replica gluing for Rényi entropies** (shown for $n = 2$). Start from the cut-and-glue kernel on each replica sheet (Fig. 1): fields are glued across $\tau = 0$ on \mathcal{B} within each sheet, while the open cut on \mathcal{A} carries independent boundary data $\Phi_{\mathcal{A},\pm}^{(j)}$. To form $\text{Tr}(\rho_{\mathcal{A}}^n)$, glue the \mathcal{A} edges cyclically across sheets, $\Phi_{\mathcal{A},-}^{(j)} = \Phi_{\mathcal{A},+}^{(j+1)}$ (with $j = n$ glued back to $j = 1$), producing the n -sheeted manifold \mathcal{M}_n and yielding $\text{Tr}(\rho_{\mathcal{A}}^n) = Z_n/(Z_1)^n$ and $S_n = (1-n)^{-1} \ln \text{Tr}(\rho_{\mathcal{A}}^n)$; the von Neumann entropy follows by analytic continuation $n \rightarrow 1$.

so that

$$\delta S_{\text{EE}}(B_R; \rho) = \int_{\mathcal{M}} d^d x \sqrt{g(x)} \mathcal{T}_{\mu\nu}^{\text{EE}}(x | B_R; \rho) \delta g^{\mu\nu}(x). \quad (19)$$

Define the trace projection

$$\mathcal{T}^{\text{EE}}(x | B_R; \rho) \equiv -2 g^{\mu\nu}(x) \mathcal{T}_{\mu\nu}^{\text{EE}}(x | B_R; \rho). \quad (20)$$

A boundary movement $B_R \rightarrow B_{R+\delta R}$ can be undone by a diffeomorphism that maps the shifted ball back to the original coordinate locus, at the price of pulling back the metric. The resulting change in the pulled-back metric is a uniform Weyl rescaling at fixed cut locus. For an infinitesimal radius change at fixed shape, $R \rightarrow R + \delta R$,

$$\delta g_{\mu\nu}(x) = 2 \frac{\delta R}{R} g_{\mu\nu}(x), \quad \delta g^{\mu\nu}(x) = -2 \frac{\delta R}{R} g^{\mu\nu}(x). \quad (21)$$

Inserting this into Eq. (19) yields

$$R \frac{dS_{\text{EE}}(B_R; \rho)}{dR} = \int_{\mathcal{M}} d^d x \sqrt{g(x)} \mathcal{T}^{\text{EE}}(x | B_R; \rho). \quad (22)$$

Because $\delta g^{\mu\nu} \propto g^{\mu\nu}$, a size flow isolates the trace channel.

At integer $n \geq 2$ the replica definition gives $S_n = (1-n)^{-1} (\ln Z_n - n \ln Z_1)$. A radius change at fixed shape is again organized by a Weyl response on \mathcal{M}_n . In particular,

$$R \frac{dS_n(B_R; \rho)}{dR} = \frac{1}{1-n} \left[\left\langle \int_{\mathcal{M}_n} d^d x \sqrt{g} T(x) \right\rangle_{\mathcal{M}_n, \rho} - n \left\langle \int_{\mathcal{M}_1} d^d x \sqrt{g} T(x) \right\rangle_{\mathcal{M}_1, \rho} \right] + \mathcal{R}_{\text{flow,ct}}^{(n)}, \quad (23)$$

where $T(x) \equiv T^\mu{}_\mu(x)$ and $\mathcal{R}_{\text{flow,ct}}^{(n)}$ denotes the UV-local and Σ -local counterterm completion fixed by the chosen replica/cut prescription and trace-renormalization scheme; see App. J. For a fixed prescription, $\mathcal{R}_{\text{flow,ct}}^{(n)}$ is state independent and therefore cancels in the vacuum subtraction defining ΔS_n and \mathfrak{s}_n .

B. Source-detector correlator

At leading order in the metric perturbation, the Rosenhaus-Smolkin identity gives [12, 13]

$$\delta S_{\text{EE}}(B_R; \rho) = -\frac{1}{2} \int_{\mathcal{M}} d^d x \sqrt{g(x)} \left\langle T_{\mu\nu}(x) K_\rho(R) \right\rangle_\rho \delta g^{\mu\nu}(x) + \delta S_{\text{EE}}^{(\text{ho})} + \delta S_{\text{EE}}^{(\text{ct})}. \quad (24)$$

Taking the trace and using Eq. (22) yields

$$R \frac{dS_{\text{EE}}(B_R; \rho)}{dR} = \int_{\mathcal{M}} d^d x \sqrt{g(x)} \left\langle T(x) K_\rho(R) \right\rangle_\rho + \mathcal{R}_{\text{flow}}^{(\text{ho})} + \mathcal{R}_{\text{flow}}^{(\text{ct})}, \quad T(x) \equiv T^\mu{}_\mu(x). \quad (25)$$

The modular Hamiltonian acts as a region-supported source tied to the cut, while the local trace insertion acts as a detector scanning the spacetime response.

C. Vacuum-subtracted radius flow

Apply Eq. (25) to $\rho = \rho_{h,\lambda}$ and to $\rho = \rho_0$ and subtract. This gives

$$\mathfrak{s}_{\text{EE}}(R; h, \lambda) = \int_{\mathcal{M}} d^d x \sqrt{g(x)} \left[\left\langle T(x) K_h(R) \right\rangle_{\rho_{h,\lambda}} - \left\langle T(x) K_{\text{vac}}(R) \right\rangle_{\rho_0} \right] + \Delta \mathcal{R}_{\text{flow}}^{(\text{ho})} + \Delta \mathcal{R}_{\text{flow}}^{(\text{ct})}, \quad (26)$$

with

$$K_h(R) \equiv -\ln \rho_{B_R, h, \lambda}, \quad K_{\text{vac}}(R) \equiv -\ln \rho_{B_R, 0}. \quad (27)$$

The exact trace-selected logic is crucial, but it does *not* by itself determine which Breit-frame GFF profile should best approximate the leading boundary coefficient after renormalization, surface isolation, and state preparation are all fixed. That bridge remains dynamical and is therefore tested empirically below. The pure scalar template is the minimal baseline because of trace selection; the spin-2 template is a competing endpoint because the holographic integrated stress-tensor response summarized in App. L is not controlled by $A^S(t)$ alone; and the mixed family closes the natural two-function basis motivated by that appendix.

V. UV REFERENCE BALL KERNEL, SURFACE LOCALIZATION, AND THE BOUNDARY-FLOW BRIDGE

For a CFT vacuum reduced to a ball, the modular Hamiltonian is local [10]:

$$K_{\text{CFT}}(R) = 2\pi \int_{|\mathbf{y}| < R} d^3 \mathbf{y} F_R(\mathbf{y}) T_{00}(0, \mathbf{y}) + c_{\text{CFT}}(R),$$

$$F_R(\mathbf{y}) \equiv \frac{R^2 - |\mathbf{y}|^2}{2R}. \quad (28)$$

In QCD this locality is not expected to hold in the IR. The role of $K_{\text{CFT}}(R)$ here is to organize the near- Σ singular structure controlling UV-local and Σ -local counterterms.

Starting from Eq. (26), add and subtract $K_{\text{CFT}}(R)$ inside the modular correlators:

$$\begin{aligned} & \langle T(x) K_h(R) \rangle_{\rho_{h, \lambda}} - \langle T(x) K_{\text{vac}}(R) \rangle_{\rho_0} \\ &= \langle T(x) K_{\text{CFT}}(R) \rangle_{\rho_{h, \lambda}} - \langle T(x) K_{\text{CFT}}(R) \rangle_{\rho_0} \\ & \quad + \langle T(x) (K_h(R) - K_{\text{CFT}}(R)) \rangle_{\rho_{h, \lambda}} \\ & \quad - \langle T(x) (K_{\text{vac}}(R) - K_{\text{CFT}}(R)) \rangle_{\rho_0}. \end{aligned} \quad (29)$$

At leading order,

$$\begin{aligned} \mathfrak{s}_{\text{EE}}(R; h, \lambda) &= 2\pi \int_{\mathcal{M}} d^d x \sqrt{g(x)} \int_{|\mathbf{y}| < R} d^{d-1} \mathbf{y} F_R(\mathbf{y}) \\ & \quad \times \left[\langle T(x) T_{00}(0, \mathbf{y}) \rangle_{\rho_{h, \lambda}} - \langle T(x) T_{00}(0, \mathbf{y}) \rangle_{\rho_0} \right] \\ & \quad + \Delta \mathcal{R}_{\text{ct}}(R) + \Delta \mathcal{R}_{\text{IR}}(R) + \Delta \mathcal{R}_{\text{fin}}(R). \end{aligned} \quad (30)$$

Define the τ -integrated trace response density

$$\tilde{\mathcal{T}}^{\text{EE}}(\mathbf{x} | B_R; \rho) \equiv \int_{-\infty}^{\infty} d\tau \mathcal{T}^{\text{EE}}(\tau, \mathbf{x} | B_R; \rho), \quad (31)$$

so that

$$R \frac{dS_{\text{EE}}(B_R; \rho)}{dR} = \int d^3 \mathbf{x} \tilde{\mathcal{T}}^{\text{EE}}(\mathbf{x} | B_R; \rho). \quad (32)$$

Vacuum subtract and renormalize in the trace channel. A minimal surface organization is

$$\begin{aligned} \Delta \tilde{\mathcal{T}}^{\text{EE, ren}}(\mathbf{x} | B_R) &= \mathcal{C}_{\Sigma}(R, \Omega; h, \lambda) \delta(r - R) \\ & \quad + \Delta \tilde{\mathcal{T}}^{\text{EE, ren, reg}}(\mathbf{x} | B_R), \end{aligned} \quad (33)$$

where the second term collects higher-derivative surface distributions together with bulk-regular terms. With this definition,

$$\mathfrak{s}_{\text{EE}}(R; h, \lambda) = c_{\Sigma}(R; h, \lambda) + \mathfrak{s}_{\text{EE}}^{\text{reg}}(R; h, \lambda), \quad (34)$$

with

$$c_{\Sigma}(R; h, \lambda) \equiv R^2 \int d\Omega \mathcal{C}_{\Sigma}(R, \Omega; h, \lambda), \quad (35)$$

and

$$\mathfrak{s}_{\text{EE}}^{\text{reg}}(R; h, \lambda) \equiv \int d^3 \mathbf{x} \Delta \tilde{\mathcal{T}}^{\text{EE, ren, reg}}(\mathbf{x} | B_R). \quad (36)$$

At integer $n \geq 2$ the analogous decomposition reads

$$\mathfrak{s}_n(R; h, \lambda) = c_{\Sigma, n}(R; h, \lambda) + \mathfrak{s}_n^{\text{reg}}(R; h, \lambda). \quad (37)$$

For practical lattice studies one works in the rest frame and averages over ball centers and lattice rotations, so the angle-integrated monopole piece is the natural quantity to compare to isotropic Breit templates. We say that a radius interval $R \in [R_1, R_2]$ is *boundary dominated* if the dominant nontrivial R dependence of the measured flow is controlled by $c_{\Sigma}(R; h)$ (or $c_{\Sigma, n}$), while the packaged remainder is subleading and/or slowly varying.

Status of assumptions and derivations. To make explicit what is definition-level versus hypothesis-level:

- *Exact on the lattice (definition-level):* for a fixed replica/cut prescription, $\Delta S_n(B_R; h)$ and $\mathfrak{s}_n(R; h)$ are well-defined lattice observables computed from replica ratios.
- *Continuum organizing principle (controlled):* a radius change at fixed shape is a Weyl rescaling, so the flow is trace selected; after trace-channel renormalization, UV structure can be organized into Σ -supported distributions plus a regular remainder.
- *Empirical hypothesis (to be tested):* on some accessible window $a \ll R \ll L/2$, the leading nontrivial R dependence is dominated by the $k = 0$ surface term and is well described by the small template basis generated by $\{A^S, A\}$ (with a low-curvature remainder accounting for smooth backgrounds and residual contact structure).

To make boundary dominance testable, we advocate the basis fit

$$\mathfrak{s}_n^{\text{lat}}(R) = a_0^{(n)} \mathfrak{t}_h^{(0)}(R) + a_2^{(n)} \mathfrak{t}_h^{(2)}(R) + r_M(R), \quad (38)$$

with

$$r_M(R) = \sum_{m=0}^M b_m R^m, \quad M = 0, 1, 2. \quad (39)$$

Here (c_0, c_2) label the abstract mixed template family introduced in Sec. VI, whereas $(a_0^{(n)}, a_2^{(n)})$ are the coefficients extracted from lattice data on a chosen window. Pure spin-0 and pure spin-2 fits are the nested limits $a_2^{(n)} = 0$ and $a_0^{(n)} = 0$. If desired, one may repackage the same fit as an overall normalization times the mixed template $\mathfrak{t}_h^{\text{mix}}(R; c_0, c_2)$, with (c_0, c_2) defined only up to an overall rescaling. The holographic fixed-ratio benchmark corresponds to the further restriction $a_0^{(n)} : a_2^{(n)} = c_0^{\text{holo}} : c_2^{\text{holo}}$.

Boundary dominance is not tied to the polynomial choice in Eq. (39); one may equally use an expansion in $(R - R_*)$ about the window midpoint, a constrained spline with a fixed smoothness prior, or a Gaussian-process smooth prior. What matters is that the extracted coefficients and turning point remain stable under such changes. To quantify the intended ‘‘low-curvature remainder’’ condition, define on a chosen window

$$c_{\text{temp}}(R) \equiv a_0^{(n)} \mathfrak{t}_h^{(0)}(R) + a_2^{(n)} \mathfrak{t}_h^{(2)}(R), \quad (40)$$

together with the dimensionless curvature measures

$$\kappa_{\text{reg}} \equiv \max_{R \in [R_1, R_2]} \left| R^2 \frac{d^2 r_M}{dR^2} \right|, \quad (41)$$

$$\kappa_{\text{temp}} \equiv \max_{R \in [R_1, R_2]} \left| R^2 \frac{d^2 c_{\text{temp}}}{dR^2} \right|. \quad (42)$$

A boundary-dominated window is one in which the coefficients remain stable under moderate changes of M , $R_{1,2}$, and the remainder basis, and in which $\kappa_{\text{reg}} \ll \kappa_{\text{temp}}$. In that sense the remainder cannot fake a template turning point without developing comparable curvature and destabilizing the fit.

VI. GRAVITATIONAL FORM FACTORS, ENDPOINT TEMPLATES, AND THE MIXED HOLOGRAPHIC BASIS

We use a minimal two-channel notation throughout this section: $A^S(t)$ denotes the scalar/trace GFF, $A(t)$ the spin-2/TT GFF, and the superscripts 0 and 2 on $\mathfrak{t}_h^{(0)}(R)$ and $\mathfrak{t}_h^{(2)}(R)$ refer to the corresponding scalar and spin-2 channels. The real-space templates are simply the associated Breit-frame densities, evaluated at the entangling radius R and multiplied by R^3 .

This section defines the Breit-frame GFF template family that will be compared to the boundary observable extracted from the entanglement flow. The scalar/trace template remains the minimal baseline because the continuum flow is trace selected, but the spin-2/TT template is also a bona fide competing endpoint, and the

natural closure is the mixed two-function basis generated by $A^S(t)$ and $A(t)$. Appendix L motivates this basis: within soft-wall holographic QCD, the pole-subtracted integrated trace-energy correlator closes on these two GFFs and on no additional low-spin structures in that model.

A. Spin-0 (trace-channel) endpoint

For each partonic sector $i \in \{q, g\}$, define the scalar (trace-channel) GFF $A_i^S(t)$ by the spin-averaged matrix element of the traced symmetric EMT:

$$\frac{1}{2S+1} \sum_{\lambda=-S}^S \langle p', \lambda | \hat{T}_{i\mu}{}^\mu(0) | p, \lambda \rangle \equiv 2M_h^2 A_i^S(t), \quad (43)$$

with $t \equiv (p' - p)^2$. The entanglement-side boundary observable extracted from lattice $\mathfrak{s}_n(R; h)$ is tied to the fixed replica prescription and to the chosen renormalized definition of the trace operator $T^\mu{}_\mu$ on the lattice. A quantitative comparison to the continuum GFF inputs therefore requires an EMT/trace renormalization and matching procedure (for example a flowed EMT matched to $\overline{\text{MS}}$ at a reference scale). In the present paper the comparison is intentionally formulated at the shape level: an overall normalization mismatch is absorbed into the fitted template coefficients, while any residual Σ -localized contact-term structure is treated as part of the low-curvature remainder sector.

The separate quark/gluon trace operators mix under renormalization; throughout we take the sector-decomposed $A_i^S(t)$ in the same renormalization scheme and scale as the numerical inputs quoted below. In Breit kinematics $\Delta^0 = 0$ one has $t = -\Delta^2$.

Define the Breit-frame three-dimensional density

$$\rho_{S,i}(r) \equiv \int \frac{d^3 \Delta}{(2\pi)^3} e^{i\Delta \cdot r} A_i^S(-\Delta^2), \quad r \equiv |r|, \quad (44)$$

and sum over $i = q, g$ to obtain $\rho_S(r)$. The corresponding dimensionless surface-evaluated template is

$$\mathfrak{t}_h^{(0)}(R) \equiv R^3 \rho_S(R). \quad (45)$$

This is the most direct Breit-frame benchmark for a trace-selected boundary observable.

B. TT/spin-2 endpoint from the A form factor

For a spin- $\frac{1}{2}$ target of mass M_h , the symmetric EMT matrix element is commonly decomposed in terms of four invariant form factors $A_i(t)$, $B_i(t)$, $D_i(t)$, and $\overline{C}_i(t)$, as in App. E. The scalar/trace channel isolates a specific combination of these form factors and leads to $A_i^S(t)$. However, the TT sector is naturally tied to the tensor part of

the stress-tensor correlator, and the simplest Breit-frame TT-inspired endpoint is built from $A_i(t)$ alone:

$$A_i(t) = \alpha_{A,i} \left(1 - \frac{t}{\Lambda_{A,i}^2} \right)^{-2}, \quad i \in \{q, g\}, \quad (46)$$

with the numerical parameters quoted below.

Define

$$\rho_{A,i}(r) \equiv \int \frac{d^3 \Delta}{(2\pi)^3} e^{i\Delta \cdot r} A_i(-\Delta^2), \quad (47)$$

and $\rho_A(r) = \rho_{A,q}(r) + \rho_{A,g}(r)$. The corresponding surface-evaluated endpoint is

$$\mathfrak{t}_h^{(2)}(R) \equiv R^3 \rho_A(R). \quad (48)$$

In the present paper we use $\mathfrak{t}_h^{(2)}(R)$ as a compact TT/spin-2 proxy. It is not dictated by trace selection alone, but it is one of the two natural basis elements singled out by the soft-wall analysis of App. L.

C. Mixed spin-0/spin-2 template and holographic benchmark

The endpoint templates do not exhaust the natural GFF hypothesis space. Appendix L shows that, within soft-wall AdS/QCD and for the pole-subtracted integrated trace-energy correlator, one obtains a definite linear combination of A^S and A . This suggests defining, for each partonic sector,

$$G_{\text{mix}i}(t; c_0, c_2) \equiv c_0 A_i^S(t) + c_2 A_i(t), \quad (49)$$

with coefficients c_0 and c_2 not fixed a priori by the lattice analysis. The corresponding Breit density is

$$\begin{aligned} \rho_{\text{mix}i}(r; c_0, c_2) &\equiv \int \frac{d^3 \Delta}{(2\pi)^3} e^{i\Delta \cdot r} G_{\text{mix}i}(-\Delta^2; c_0, c_2) \\ &= c_0 \rho_{S,i}(r) + c_2 \rho_{A,i}(r), \end{aligned} \quad (50)$$

and after summing over $i = q, g$ one obtains the mixed boundary template

$$\mathfrak{t}_h^{\text{mix}}(R; c_0, c_2) \equiv R^3 \rho_{\text{mix}}(R; c_0, c_2) = c_0 \mathfrak{t}_h^{(0)}(R) + c_2 \mathfrak{t}_h^{(2)}(R). \quad (51)$$

Because a common rescaling of (c_0, c_2) can be absorbed into an overall normalization, only their ratio matters at the level of shape matching. In practice it is therefore cleaner to fit the equivalent linear basis coefficients multiplying $\mathfrak{t}_h^{(0)}$ and $\mathfrak{t}_h^{(2)}$ directly, as in Eq. (38).

The soft-wall holographic derivation of App. L provides a benchmark subfamily of this mixed basis. There one finds, up to the common prefactor $1/(2\kappa_5^2) \sim N_c^2$,

$$c_2^{\text{holo}}(E_h, M_h) = 1 - \frac{1}{3} \frac{M_h^2}{E_h^2}, \quad c_0^{\text{holo}}(E_h, M_h) = -\frac{9}{32} \frac{M_h^2}{E_h^2}, \quad (52)$$

so that the fixed-ratio holographic benchmark is

$$\mathfrak{t}_h^{\text{hol}}(R; E_h, M_h) \equiv \mathfrak{t}_h^{\text{mix}}(R; c_0^{\text{holo}}(E_h, M_h), c_2^{\text{holo}}(E_h, M_h)). \quad (53)$$

In the rest/Breit kinematics $E_h = M_h$, this becomes the specific ratio $c_2^{\text{holo}} : c_0^{\text{holo}} = 2/3 : -9/32$. We emphasize that this ratio is *not* imposed in the lattice comparison: it is only a model-dependent benchmark, while the mixed coefficients are extracted freely from the data.

The logic is diagrammatic. The mixed correlator $\langle O_h T T^{00} O_h \rangle$ decomposes into s -, u -, local contact-, and t -channel Witten diagrams, shown in Fig. 10. After elastic pole subtraction and the exact integrated projection $q_1 = 0$, the s - and u -channel graphs vanish identically, leaving only TT and spin-0 t -channel exchange. Their spectral functions are precisely the hadronic GFFs $A(t)$ and $A^S(t)$. This is why the mixed fit basis $\{\mathfrak{t}_h^{(0)}, \mathfrak{t}_h^{(2)}\}$ is natural: it is the real-space image of the two GFF channels selected in the soft-wall analysis.

Scope of the benchmark. The soft-wall fixed-ratio benchmark is used only as a *model-dependent* one-parameter subfamily inside the broader mixed fit; it is not claimed to be universal, and it is not imposed on lattice data (the lattice comparison leaves the coefficients free and extracts them from the measured flow).

D. Why the comparison is boundary evaluated

On the entanglement side, the boundary observable $c_\Sigma(R; h)$ entering Eq. (34) is defined by isolating the leading $\delta(r - R)$ surface distribution in the renormalized response. This motivates comparing $c_\Sigma(R; h)$ to a *local* isotropic radial profile evaluated at the same radius $r = R$ rather than to an integrated interior quantity. The particular power of R in (45), (48), and (51) is chosen only to form a dimensionless template in three spatial dimensions; any normalization mismatch is absorbed into the fitted coefficients.

For later diagnostics it is useful to define an explicit interior/bulk proxy built from any of the densities $\rho_X(r)$,

$$c_h^{\text{bulk},X}(R) \equiv \int_0^R dr r^2 \rho_X(r), \quad X \in \{0, 2, \text{mix}\}, \quad (54)$$

which is manifestly smooth/monotone for positive dipole densities.

E. Dipole ansatz, closed forms, and numerical inputs

For the scalar/trace endpoint we use

$$A_i^S(t) = \alpha_{S,i} \left(1 - \frac{t}{\Lambda_{S,i}^2} \right)^{-2}, \quad i \in \{q, g\}. \quad (55)$$

Then, in Breit kinematics,

$$A_i^S(-\Delta^2) = \alpha_{S,i} \left(1 + \frac{\Delta^2}{\Lambda_{S,i}^2} \right)^{-2}, \quad (56)$$

and the Fourier transform is elementary:

$$\rho_{S,i}(r) = \alpha_{S,i} \frac{\Lambda_{S,i}^3}{8\pi} e^{-\Lambda_{S,i} r}. \quad (57)$$

Hence

$$\mathfrak{t}_h^{(0)}(R) = R^3 \sum_{i=q,g} \alpha_{S,i} \frac{\Lambda_{S,i}^3}{8\pi} e^{-\Lambda_{S,i} R}. \quad (58)$$

For the TT/spin-2 endpoint,

$$A_i(t) = \alpha_{A,i} \left(1 - \frac{t}{\Lambda_{A,i}^2} \right)^{-2}, \quad (59)$$

so that

$$\rho_{A,i}(r) = \alpha_{A,i} \frac{\Lambda_{A,i}^3}{8\pi} e^{-\Lambda_{A,i} r}, \quad (60)$$

$$\mathfrak{t}_h^{(2)}(R) = R^3 \sum_{i=q,g} \alpha_{A,i} \frac{\Lambda_{A,i}^3}{8\pi} e^{-\Lambda_{A,i} R}. \quad (61)$$

Because the transform is linear, the mixed family is simply

$$\begin{aligned} \mathfrak{t}_h^{\text{mix}}(R; c_0, c_2) &= c_0 \mathfrak{t}_h^{(0)}(R) + c_2 \mathfrak{t}_h^{(2)}(R) \\ &= R^3 \sum_{i=q,g} \left[c_0 \alpha_{S,i} \frac{\Lambda_{S,i}^3}{8\pi} e^{-\Lambda_{S,i} R} + c_2 \alpha_{A,i} \frac{\Lambda_{A,i}^3}{8\pi} e^{-\Lambda_{A,i} R} \right]. \end{aligned} \quad (62)$$

For the holographic benchmark $\mathfrak{t}_h^{\text{hol}}$, one substitutes the fixed coefficients in Eq. (52). The two pure endpoints therefore remain the essential reference shapes, while the mixed family interpolates between them (or, if one coefficient changes sign, distorts them in a controlled way determined by the data).

We use representative lattice-driven dipole parameters from Refs. [46] as repackaged in Ref. [41]:

a. Trace-channel (spin-0) inputs.

$$\begin{aligned} \alpha_{S,q} = 0.510, \quad \alpha_{S,g} = 0.501, \quad \Lambda_{S,q} = 0.804 \text{ GeV}, \\ \Lambda_{S,g} = 0.596 \text{ GeV}. \end{aligned} \quad (63)$$

b. Spin-2 (A-form-factor) inputs.

$$\begin{aligned} \alpha_{A,q} = 0.510, \quad \alpha_{A,g} = 0.501, \quad \Lambda_{A,q} = 1.477 \text{ GeV}, \\ \Lambda_{A,g} = 1.262 \text{ GeV}. \end{aligned} \quad (64)$$

The scalar and spin-2 endpoint templates both display a single pronounced maximum and hence a single sign

TABLE I. Dipole fit parameters used for the Breit-frame templates in this work.

Channel	α_q	α_g	Λ_q [GeV]	Λ_g [GeV]
Spin-0 / trace $A^S(t)$	0.510	0.501	0.804	0.596
Spin-2 / TT $A(t)$	0.510	0.501	1.477	1.262

change of the derivative. For a single dipole component $R^3 e^{-\Lambda R}$ the maximum lies at $R = 3/\Lambda$. For the two-component positive sums above, one finds

$$0.74 \text{ fm} \lesssim R_{\text{EE}}^{(0)} \lesssim 0.99 \text{ fm}, \quad (65)$$

while for the spin-2 endpoint

$$0.40 \text{ fm} \lesssim R_{\text{EE}}^{(2)} \lesssim 0.47 \text{ fm}, \quad (66)$$

with the representative two-component numerical value

$$R_{\text{EE}}^{(2)} \simeq 2.189 \text{ GeV}^{-1} \simeq 0.432 \text{ fm}. \quad (67)$$

The mixed family does not have a unique turning point until the coefficients are fitted, which is precisely why the two pure endpoints remain useful: they furnish fixed hadronic scales against which the mixed fit can be interpreted.

The pure endpoint shapes are shown in Figs. 6-9. In particular, the standalone spin-2 plots in Figs. 8 and 9 are included because the pure TT endpoint scale $R_{\text{EE}}^{(2)}$ is one of the sharpest diagnostics in the later lattice discrimination test. The Witten-diagram decomposition underpinning the mixed basis is displayed in Fig. 10; the detailed derivation is deferred to App. L.

VII. MAIN LATTICE-FACING HYPOTHESES, MIXED-BASIS FITS, AND FALSIFIABILITY

Section V motivates a boundary-dominated window in which the leading nontrivial R dependence is carried by $c_{\Sigma,n}(R; h)$ and the packaged remainder is subleading and low curvature.

a. Mixed-basis hypothesis. On such a window, the working lattice hypothesis is

$$c_{\Sigma,n}(R; h) \approx a_0^{(n)} \mathfrak{t}_h^{(0)}(R) + a_2^{(n)} \mathfrak{t}_h^{(2)}(R), \quad (68)$$

with pure spin-0 and pure spin-2 endpoint models recovered as the nested limits $a_2^{(n)} = 0$ and $a_0^{(n)} = 0$. A stable mixed fit with both coefficients nonzero is therefore itself a nontrivial physical outcome.

b. Holographic fixed-ratio benchmark. A useful one-parameter subfamily is obtained by constraining the ratio of the two basis coefficients to the soft-wall benchmark,

$$a_0^{(n)} : a_2^{(n)} = c_0^{\text{hol}} : c_2^{\text{hol}}. \quad (69)$$

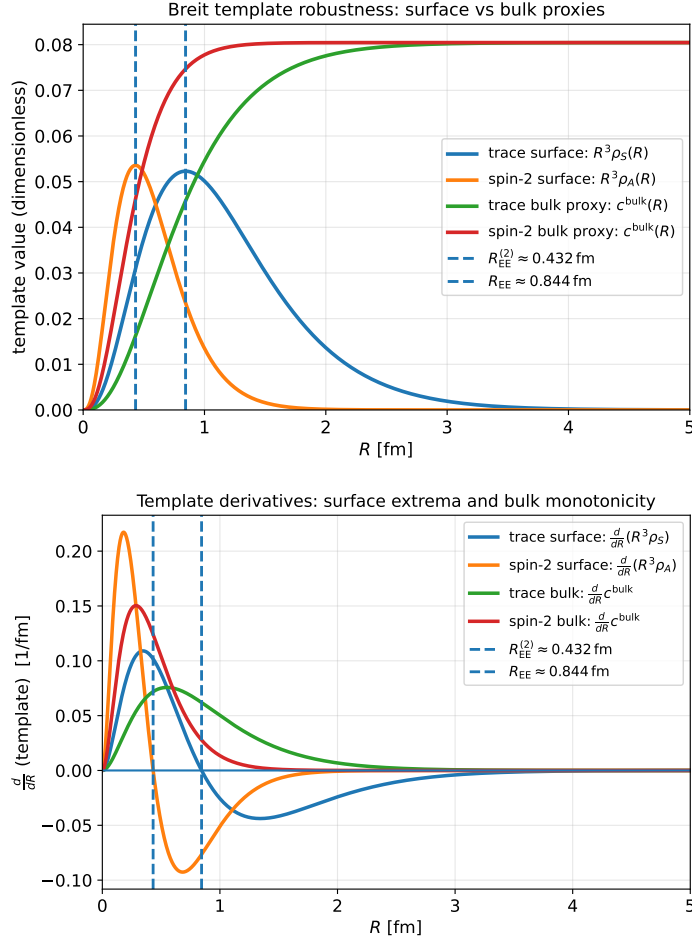


FIG. 4. **Spin-0 and spin-2 endpoint templates and bulk proxies.** Top: the spin-0/trace endpoint $t_h^{(0)}(R) = R^3 \rho_S(R)$ and the spin-2 endpoint $t_h^{(2)}(R) = R^3 \rho_A(R)$, together with the interior proxies from Eq. (54). Bottom: their derivatives. The surface-evaluated endpoints have a single pronounced extremum, whereas the interior proxies remain smooth and monotone for positive dipole densities. These endpoint curves (shown here for the representative dipole inputs used in this work) form the basis of the mixed family $t_h^{\text{mix}}(R; c_0, c_2)$.

Equivalently, one may fit a single overall amplitude multiplying $t_h^{\text{ho}}(R; E_h, M_h)$. This constraint is used only as a benchmark test rather than as an input assumption.

The sharp content is therefore the R dependence, not the absolute normalization. Because the fitted coefficients are unconstrained in sign, the corresponding boundary-dominated feature in the data can appear as either a peak or a dip at the turning point of the preferred template.

Define the first positive extrema of the pure endpoints,

$$\left. \frac{dt_h^{(0)}(R)}{dR} \right|_{R=R_{EE}^{(0)}} = 0, \quad \left. \frac{dt_h^{(2)}(R)}{dR} \right|_{R=R_{EE}^{(2)}} = 0. \quad (70)$$

For the representative dipole inputs,

$$R_{EE}^{(0)} \simeq 0.84 \text{ fm}, \quad R_{EE}^{(2)} \simeq 0.43 \text{ fm}. \quad (71)$$

A stable boundary-dominated lattice signal can therefore discriminate between the two pure endpoints at the level

of hadronic radii, while a successful mixed fit can be interpreted relative to these two anchor scales.

Define the sign-sensitive gradient diagnostics for the pure endpoints,

$$\mathcal{G}_0(R) \equiv -\frac{dt_h^{(0)}(R)}{dR}, \quad \mathcal{G}_2(R) \equiv -\frac{dt_h^{(2)}(R)}{dR}. \quad (72)$$

Each changes sign at its own turning point. The corresponding sign change seen in the data is therefore informative only together with the location of the turning point and the stability of the fit under template changes. A sign change near 0.84 fm supports the spin-0 endpoint. A sign change near 0.43 fm supports the spin-2 endpoint. A stable turning point in between, together with nonzero fitted weights for both basis elements, indicates genuine mixing.

The default lattice-facing fit model on each candidate window is the mixed-basis-plus-remainder ansatz of Eqs. (38) and (39). Because the pure endpoints are

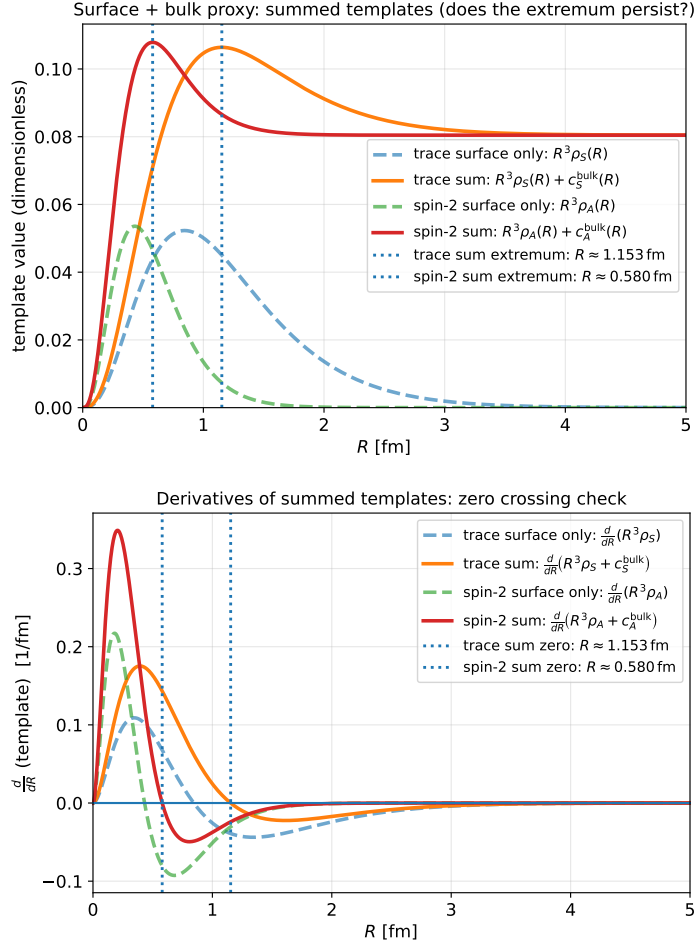


FIG. 5. **Surface-plus-bulk distortions of the endpoint templates.** Top: the spin-0 and spin-2 surface-evaluated endpoints together with corresponding surface-plus-bulk proxies. Bottom: their derivatives. Adding a smooth bulk component can shift the first extremum, but it does not generate new oscillatory structure. This is why a low-curvature remainder is not expected to fake a stable turning point associated with the wrong GFF channel. These plots are illustrative for the dipole inputs adopted here and are not intended as general theorems.

nested inside this family, standard nested-model comparisons (likelihood-ratio, information criteria, or Bayes factors) are natural diagnostics in addition to the stability tests. A convincing boundary-dominated window is one in which (i) the extracted coefficients and turning point are stable under changes of M , (ii) they are stable under moderate shifts of $R_{1,2}$, (iii) they are stable under changes of lattice spacing, volume, and ball discretization, (iv) the residuals show no additional extrema or oscillations beyond statistical fluctuations, and (v) the preferred endpoint/mixed classification is itself stable under these variations.

This turns the physics question into a clean basis-selection problem. Several distinct outcomes are possible:

1. *Pure spin-0 success:* the nested fit prefers $a_2^{(n)} = 0$ within uncertainties, while $a_0^{(n)} \neq 0$ is stable. This supports the minimal trace-selected endpoint picture.

2. *Pure spin-2 success:* the nested fit prefers $a_0^{(n)} = 0$ within uncertainties, while $a_2^{(n)} \neq 0$ is stable. This supports a spin-2-dominant boundary response and aligns naturally with the holographic selector logic of App. L.
3. *Genuine mixed success:* both $a_0^{(n)}$ and $a_2^{(n)}$ are nonzero and stable, and freeing the second coefficient materially improves the fit relative to both pure endpoints. This indicates that the boundary response is genuinely mixed in GFF space.
4. *Holographic-ratio success:* the mixed fit is successful and the extracted ratio $a_0^{(n)} : a_2^{(n)}$ is consistent, within uncertainties, with the soft-wall benchmark. This would be a particularly sharp outcome, though not one assumed anywhere in the analysis.
5. *No stable GFF-basis description:* none of the endpoint or mixed fits survives the win-

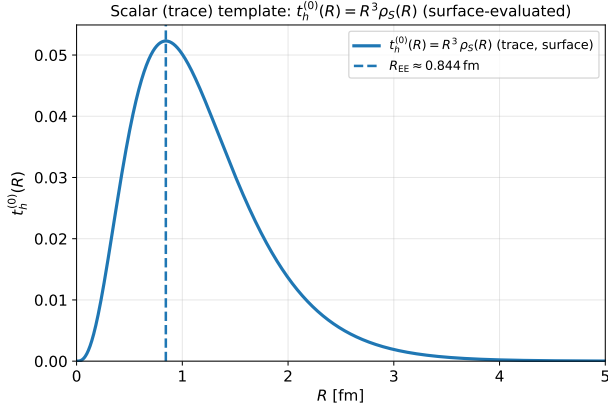


FIG. 6. **Spin-0/trace endpoint template** $t_h^{(0)}(R) = R^3 \rho_S(R)$ for the representative nucleon dipole inputs of Table I, obtained from the scalar GFF via Eqs. (44) and (45) and the dipole ansatz Eq. (55). The horizontal axis is displayed in fm by reinstating $\hbar c = 0.1973269804$ GeV fm.

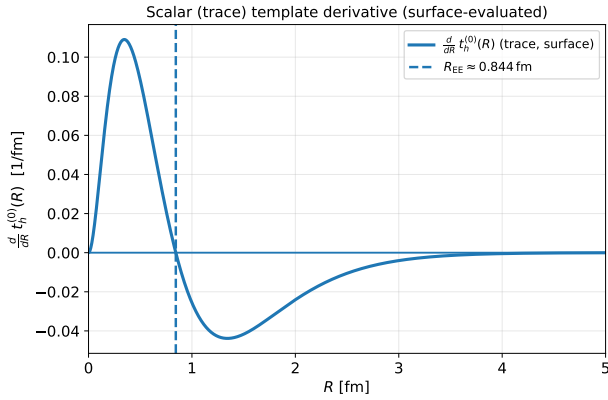


FIG. 7. **Derivative of the spin-0/trace endpoint template** for the representative nucleon dipole inputs of Table I. The first zero crossing defines $R_{EE}^{(0)}$ for the scalar endpoint.

dow/remainder/systematics tests. Then either the boundary-dominance assumption or the GFF-matching conjecture itself fails in the accessible window.

Concrete falsifiers therefore include:

- **No stable window:** there is no interval where the mixed-basis-plus-low-curvature description is stable.
- **Shape mismatch:** the lattice-inferred boundary contribution exhibits nodes, oscillations, or additional extrema not reproduced by any stable linear combination of $t_h^{(0)}$ and $t_h^{(2)}$.
- **Coefficient instability:** the extracted weights $a_0^{(n)}$ and $a_2^{(n)}$ vary strongly under changes of window, remainder basis, or lattice spacing.

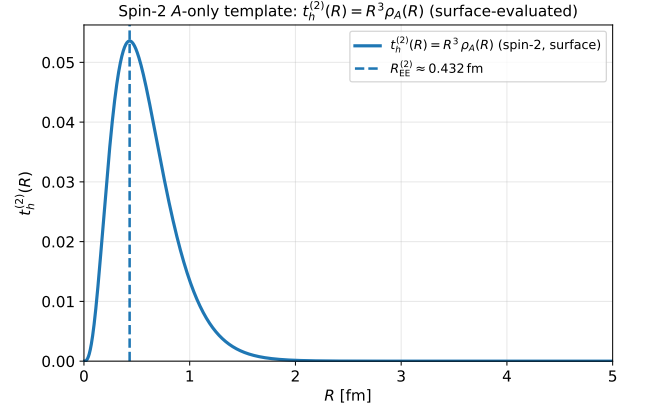


FIG. 8. **Spin-2 endpoint template** $t_h^{(2)}(R) = R^3 \rho_A(R)$ for the representative nucleon dipole inputs of Table I, obtained from the spin-2 GFF via Eqs. (47) and (48) and the dipole ansatz Eq. (59). The horizontal axis is displayed in fm by reinstating $\hbar c = 0.1973269804$ GeV fm.

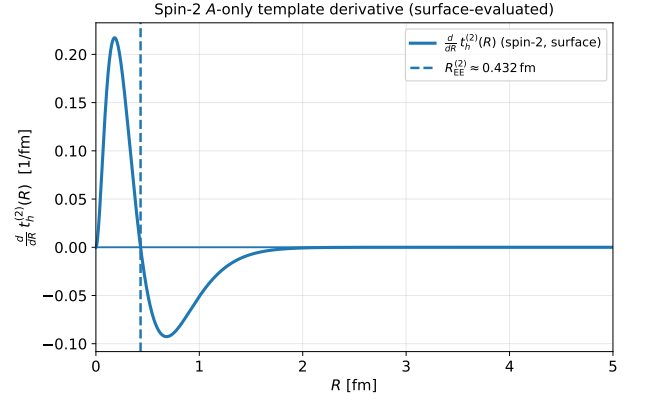


FIG. 9. **Derivative of the spin-2 endpoint template** for the representative nucleon dipole inputs of Table I. The first zero crossing defines $R_{EE}^{(2)}$ for the spin-2 endpoint.

- **Incompatible turning point:** the extracted turning point is robust but does not match either endpoint scale and cannot be reproduced by a controlled mixed interpolation.

In that sense the GFF program advocated here is sharper than a one-template-only proposal: the relative success or failure of the scalar endpoint, the spin-2 endpoint, and the genuinely mixed fit is itself an observable statement about the hadron-state entanglement response.

VIII. CONCLUSIONS AND OUTLOOK

We introduced a lattice-facing entanglement observable for QCD hadrons: the vacuum-subtracted radius flow of ball Rényi entropies in a rest-frame momentum-projected hadron state, with polarization averaging performed at the level of the final flow. At fixed replica/cut

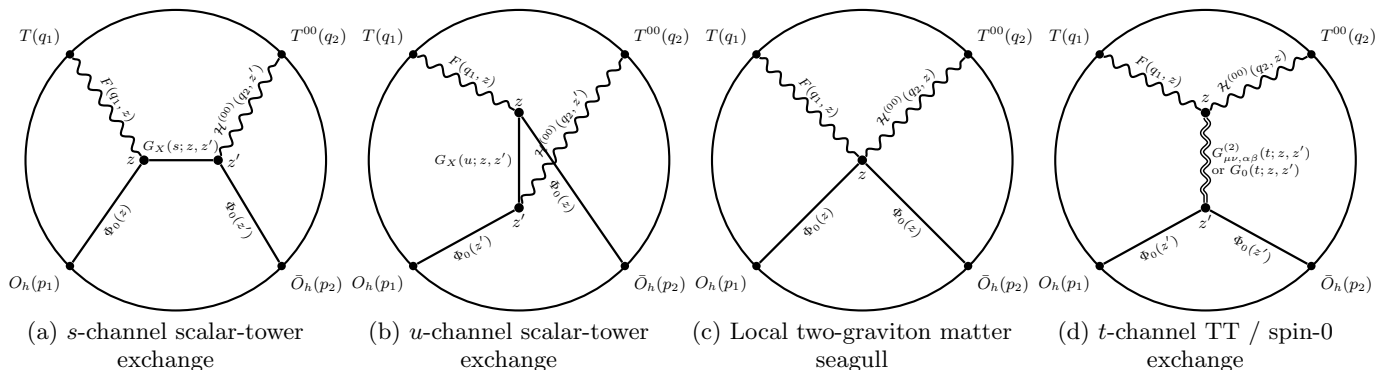


FIG. 10. **Witten-diagram decomposition underlying the mixed GFF basis.** The soft-wall correlator $\langle O_h T T^{00} O_h \rangle$ receives s - and u -channel scalar exchange, a local two-graviton seagull, and t -channel TT or spin-0 exchange. After elastic pole subtraction and the exact integrated projection $q_1 = 0$, the pole-subtracted s - and u -channels vanish, so the nonlocal regular amplitude is carried by the TT and spin-0 t -channel exchanges alone. This is why the lattice template basis closes on $A(t)$ and $A^S(t)$; details are given in App. L.

prescription this definition is exact, and vacuum subtraction removes state-independent UV and Σ -localized contributions.

A size variation at fixed shape is a Weyl response, so the continuum flow is trace selected. This motivates the modular-correlator representation developed above and, after renormalization, a surface-plus-remainder organization on $\Sigma = \partial B_R$. Operationally, boundary dominance is tested by fitting the lattice flow to the mixed-basis ansatz Eqs. (38) and (39) and checking stability against window choice, remainder choice, lattice spacing, volume, and ball discretization.

The lattice comparison is framed in the two-function GFF basis $\{t_h^{(0)}, t_h^{(2)}\}$. The pure spin-0 and pure spin-2 templates are nested limits of the mixed fit. For the representative nucleon inputs used here, the pure endpoints predict distinct turning-point scales, $R_{\text{EE}}^{(0)} \simeq 0.84$ fm and $R_{\text{EE}}^{(2)} \simeq 0.43$ fm. A stable lattice signal can therefore help distinguish among scalar dominance, spin-2 dominance, and genuine mixing.

The next step is straightforward: measure $\Delta S_n(B_R; h)$ and $\mathfrak{s}_n(R; h)$, beginning with $n = 2$, isolate a candidate boundary-dominated window, and confront the extracted shape with the two pure endpoints and the mixed fit. The outcome is data-driven. What this paper provides is the observable, the response framework, the stability protocol, and a disciplined two-function hypothesis space for lattice QCD to test.

ACKNOWLEDGMENTS

I thank Christian Weiss and Peter Schweitzer for discussions. I also thank Jefferson Lab for hospitality during the completion of this work. This work was supported by DOE grant no. DE-FG02-04ER41309, NSF grant no. 2412625, and DOE under the umbrella of the Quark-Gluon Tomography (QGT) Topical Collaboration with

Award No. DE-SC002364.

Appendix A: Rosenhaus-Smolkin identity

The leading source-detector identity used in Sec. IV, Eq. (24), is standard. It follows from combining the metric variation of the Euclidean action with the linearized entropy variation $\delta S = \text{Tr}(\delta \hat{\rho} \hat{K})$ for $\hat{K} = -\ln \hat{\rho}$. Detailed derivations are given in Refs. [12, 13].

Appendix B: Cut-and-glue and replica gluing in a solvable example

For readers who want an explicit benchmark of the cut-and-glue prescription in a setting where everything can be written in closed form, worked examples for free fields are given in Refs. [27, 42]. For integer $n \geq 2$, the replica construction glues n copies cyclically along \mathcal{A} to form the n -sheeted manifold \mathcal{M}_n branched over the entangling surface $\Sigma = \partial \mathcal{A}$ and yields

$$\text{Tr}(\rho_{\mathcal{A},0}^n) = \frac{Z_n}{(Z_1)^n}, \quad S_n(\mathcal{A}) = \frac{1}{1-n} \left(\ln Z_n - n \ln Z_1 \right). \quad (\text{B1})$$

Appendix C: Ball modular Hamiltonian in a CFT vacuum

For a half-space, Bisognano-Wichmann implies locality of the vacuum modular Hamiltonian [47]. A conformal map carries the half-space to the ball in a CFT vacuum, yielding Eq. (28) [10]. The scale $T_{\text{ent}} = 1/(2\pi R)$ is modular, not a physical temperature.

Appendix D: Trace-channel surface localization for a ball

This appendix spells out why the UV-sensitive part of the trace-channel response can be organized by distributions supported on the entangling surface $\Sigma = \partial B_R$, with a residual regular remainder.

1. Why the trace response localizes on Σ

In the correlator-based representation of the radius flow, the modular insertion associated with the UV reference ball kernel is a ball-weighted insertion of T_{00} with the characteristic factor

$$f_R(\mathbf{y}) \equiv F_R(\mathbf{y}) \Theta(R - |\mathbf{y}|), \quad F_R(\mathbf{y}) = \frac{R^2 - |\mathbf{y}|^2}{2R}. \quad (\text{D1})$$

The only nonsmooth feature of f_R is the step function $\Theta(R - |\mathbf{y}|)$. At short spatial separations, stress-tensor correlators admit a distributional/OPE organization. As a distribution in $\mathbf{x} - \mathbf{y}$ one expects

$$\langle T(0, \mathbf{x}) T_{00}(0, \mathbf{y}) \rangle \sim \sum_{n \geq 0} \mathcal{K}^{(n)}(\mathbf{x}) \partial^{(n)} \delta^{(3)}(\mathbf{x} - \mathbf{y}), \quad (\text{D2})$$

where $\partial^{(n)}$ denotes a multi-derivative acting on the delta distribution and the coefficients $\mathcal{K}^{(n)}$ are local operator expectation values. When such singular terms are integrated against f_R , derivatives of the delta distribution are transferred onto f_R in the sense of distributions. Because F_R is smooth, the only source of surface support is differentiation of the step function, producing $\delta(r - R)$ and its radial derivatives.

$$\langle p', S' | \hat{T}^{\mu\nu}(0) | p, S \rangle = \bar{u}(p', S') \left[A(t) \gamma^{\{\mu} P^{\nu\}} + \frac{B(t)}{2M_h} P^{\{\mu} i\sigma^{\nu\}\rho} \Delta_\rho + \frac{D(t)}{4M_h} (\Delta^\mu \Delta^\nu - g^{\mu\nu} \Delta^2) + \bar{C}(t) g^{\mu\nu} \right] u(p, S), \quad (\text{E1})$$

with $P = (p' + p)/2$, $\Delta = p' - p$, and $t = \Delta^2$. Contracting with $g_{\mu\nu}$ isolates the spin-0/trace channel. More broadly, GFFs parameterize EMT matrix elements and encode information often phrased in terms of the hadron mass, spin, and mechanical (pressure/shear) structure [48–60]; they have also been related to, and in phenomenological analyses constrained/extracted from, observables in near-threshold J/ψ production and DVCS [52, 61–69].

2. Renormalized distributional structure

Define the renormalized response tensor by subtracting the UV-local and Σ -local counterterms fixed by the chosen replica/cut prescription,

$$\mathcal{T}_{\mu\nu}^{\text{EE,ren}} \equiv \mathcal{T}_{\mu\nu}^{\text{EE}} - \mathcal{T}_{\mu\nu}^{\text{EE,(ct)}}. \quad (\text{D3})$$

The relevant object for the flow is the τ -integrated trace response,

$$\begin{aligned} \tilde{\mathcal{T}}^{\text{EE,ren}}(\mathbf{x} | B_R; \rho) &= \int_{-\infty}^{\infty} d\tau \mathcal{T}^{\text{EE,ren}}(\tau, \mathbf{x} | B_R; \rho), \\ \mathcal{T}^{\text{EE,ren}} &\equiv -2g^{\mu\nu} \mathcal{T}_{\mu\nu}^{\text{EE,ren}}. \end{aligned} \quad (\text{D4})$$

Locality and rotational covariance imply that at fixed R

$$\begin{aligned} \tilde{\mathcal{T}}^{\text{EE,ren}}(\mathbf{x} | B_R; \rho) &= \sum_{k=0}^{k_{\max}} \mathcal{C}^{(k)}(R, \Omega; \rho) \partial_r^k \delta(r - R) \\ &\quad + \tilde{\mathcal{T}}^{\text{EE,ren,reg}}(\mathbf{x} | B_R; \rho), \end{aligned} \quad (\text{D5})$$

where $\tilde{\mathcal{T}}^{\text{EE,ren,reg}}$ is UV finite and regular in \mathbf{x} . Vacuum subtraction preserves the same structure. This motivates the minimal surface isolation used in the main text: isolate the $k = 0$ term and package everything else into the generalized remainder.

Appendix E: Hadron EMT decomposition and kinematic limits

For a spin- $\frac{1}{2}$ target the standard symmetric EMT decomposition is

Appendix F: Breit-frame analytic formulas for dipole templates

For the dipole ansatz

$$A_i^S(-\Delta^2) = \alpha_{S,i} \left(1 + \frac{\Delta^2}{\Lambda_{S,i}^2} \right)^{-2}, \quad (\text{F1})$$

$$A_i(-\Delta^2) = \alpha_{A,i} \left(1 + \frac{\Delta^2}{\Lambda_{A,i}^2} \right)^{-2}, \quad (\text{F2})$$

one has

$$\rho_{S,i}(r) = \alpha_{S,i} \frac{\Lambda_{S,i}^3}{8\pi} e^{-\Lambda_{S,i} r}, \quad \rho_{A,i}(r) = \alpha_{A,i} \frac{\Lambda_{A,i}^3}{8\pi} e^{-\Lambda_{A,i} r}. \quad (\text{F3})$$

Therefore

$$\mathbf{t}_h^{(0)}(R) = R^3 \rho_S(R), \quad \mathbf{t}_h^{(2)}(R) = R^3 \rho_A(R), \quad (\text{F4})$$

and

$$\frac{d\mathbf{t}_h^{(0)}}{dR} = 3R^2 \rho_S'(R) + R^3 \rho_S''(R), \quad (\text{F5})$$

$$\frac{d\mathbf{t}_h^{(2)}}{dR} = 3R^2 \rho_A'(R) + R^3 \rho_A''(R). \quad (\text{F6})$$

In the mixed family,

$$\mathbf{t}_h^{\text{mix}}(R; c_0, c_2) = c_0 \mathbf{t}_h^{(0)}(R) + c_2 \mathbf{t}_h^{(2)}(R), \quad (\text{F7})$$

and for the fixed holographic benchmark one simply inserts the coefficients from Eq. (52). The mixed family therefore does not introduce any new Fourier-transform technology beyond linear superposition of the two pure endpoints.

Appendix G: CFT benchmark on a sphere

For a QFT on Euclidean S^d of radius R in a maximally symmetric vacuum state, the entangling surface may be chosen as the equator. The modular Hamiltonian is then local and generated by the corresponding Killing vector [10, 70]. A constant Weyl rescaling of the S^d metric is equivalent to R rescaling and leads to

$$R \frac{dS_{\text{EE}}}{dR} = \frac{\Omega_d R^{d+1}}{d} \frac{d}{dR} \left(\frac{C}{R^d} \right), \quad (\text{G1})$$

where C is the coefficient of the stress-tensor one-point function on the sphere. The spectral representation of the conserved correlator shows explicitly that only the spin-0 sector contributes to trace-channel correlators.

Appendix H: Toy model: smooth “which-side” occupancy background

Ignore UV entanglement across the cut and keep only the binary occupation of B_R versus its complement. The reduced density matrix is

$$\rho_{B_R}^{\text{occ}} = f(R) |1\rangle\langle 1| + [1 - f(R)] |0\rangle\langle 0|, \\ f(R) \equiv \frac{\text{Vol}(B_R)}{\text{Vol}(\Sigma_{\text{tot}})} \simeq \frac{4\pi R^3}{3L^3} \quad (R \ll L). \quad (\text{H1})$$

This gives smooth R dependence with no hadronic scale. For example,

$$R \frac{d}{dR} S_{\text{EE}}^{\text{occ}}(R) = 3f(R) \ln \frac{1-f(R)}{f(R)},$$

which is smooth for $a \ll R \ll L/2$. Thus occupancy backgrounds belong naturally in the low-curvature remainder sector.

Appendix I: Wave-packet imaging of local EMT observables (optional)

For a normalizable wave packet,

$$|\Psi, \lambda\rangle = \int \frac{d^3\mathbf{p}}{2E_{\mathbf{p}}(2\pi)^3} \psi(\mathbf{p}) |\mathbf{p}, \lambda\rangle, \quad \int \frac{d^3\mathbf{p}}{2E_{\mathbf{p}}(2\pi)^3} |\psi(\mathbf{p})|^2 = 1, \quad (\text{I1})$$

translation covariance yields the equal-time imaging identity for a local operator $\hat{\mathcal{O}}(0)$:

$$\left\langle \hat{\mathcal{O}}(0, \mathbf{x}) \right\rangle_{\rho_{\Psi, \lambda}} = \int \frac{d^3\mathbf{P}}{(2\pi)^3} \int \frac{d^3\mathbf{\Delta}}{(2\pi)^3} \mathcal{W}(\mathbf{P}, \mathbf{\Delta}) e^{-i\mathbf{\Delta} \cdot \mathbf{x}} \\ \times \langle p', \lambda | \hat{\mathcal{O}}(0) | p, \lambda \rangle, \quad (\text{I2})$$

where

$$\mathcal{W}(\mathbf{P}, \mathbf{\Delta}) \equiv \frac{\psi^*(\mathbf{P} + \mathbf{\Delta}/2) \psi(\mathbf{P} - \mathbf{\Delta}/2)}{4E_{\mathbf{P} + \mathbf{\Delta}/2} E_{\mathbf{P} - \mathbf{\Delta}/2}}. \quad (\text{I3})$$

All entanglement observables in the main text are nevertheless defined directly for the rest-frame momentum-projected state.

Appendix J: Integer- n trace flow versus the $n \rightarrow 1$ modular-correlator form

At fixed integer Rényi index $n \geq 2$ the radius flow is naturally expressed in terms of an integrated trace one-point function on the n -sheeted replica manifold \mathcal{M}_n , whereas an explicit modular Hamiltonian insertion appears only after taking the von Neumann limit $n \rightarrow 1$. For integer n ,

$$S_n(B_R; \rho) = \frac{1}{1-n} \left(\ln Z_n[B_R; \rho] - n \ln Z_1[\rho] \right). \quad (\text{J1})$$

Under a background-metric variation,

$$\delta \ln Z_n[B_R; \rho] = -\frac{1}{2} \left\langle \int_{\mathcal{M}_n} d^d x \sqrt{g} T_{\mu\nu}(x) \delta g^{\mu\nu}(x) \right\rangle_{\mathcal{M}_n, \rho} \\ + \delta \ln Z_n^{\text{(ct)}}. \quad (\text{J2})$$

A Weyl rescaling with the cut locus held fixed gives

$$R \frac{dS_n(B_R; \rho)}{dR} = \frac{1}{1-n} \left[\left\langle \int_{\mathcal{M}_n} d^d x \sqrt{g} T(x) \right\rangle_{\mathcal{M}_n, \rho} \right. \\ \left. - n \left\langle \int_{\mathcal{M}_1} d^d x \sqrt{g} T(x) \right\rangle_{\mathcal{M}_1, \rho} \right] + \mathcal{R}_{\text{flow, ct}}^{(n)}(R). \quad (\text{J3})$$

The modular Hamiltonian $K_\rho(R) = -\ln \rho_{B_R}$ enters only in the $n \rightarrow 1$ limit because

$$\delta S_{\text{EE}}(B_R; \rho) = \text{Tr}_{B_R}(\delta \rho_{B_R} K_\rho(R)). \quad (\text{J4})$$

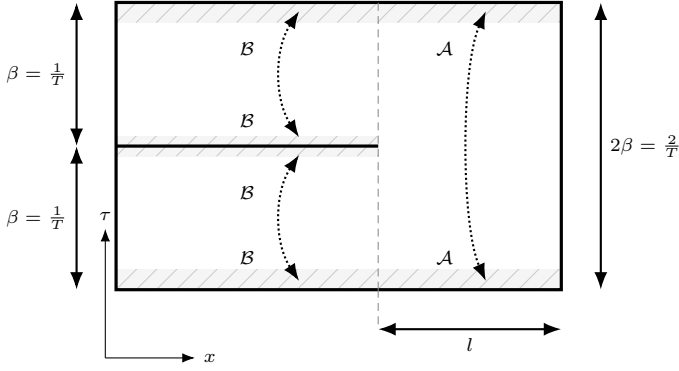


FIG. 11. **Thermal (replica) implementation of $\text{Tr}(\rho_{\mathcal{A}}^n)$ on the lattice (shown for $n = 2$).** In the replica construction, the subsystem \mathcal{A} is evolved around the Euclidean-time circle with period $n\beta$, while the complement \mathcal{B} remains β periodic on each replica sheet. For $n = 2$ this is represented by a single geometry in which \mathcal{A} has temporal extent 2β , whereas \mathcal{B} splits into two independent β -periodic slabs. This picture is equivalent to the cut-and-glue replica manifold used to evaluate $\text{Tr}(\rho_{\mathcal{A}}^2) = Z_2/Z_1^2$ in the Buividovich-Polikarpov method [18].

Equivalently, the replica derivative produces $\ln \rho_{B_R}$:

$$\partial_n \rho_{B_R}^n \Big|_{n=1} = \rho_{B_R} \ln \rho_{B_R}. \quad (\text{J5})$$

A useful bridge identity is [13, 71]

$$\partial_n \langle \mathcal{O} \rangle_n \Big|_{n=1} = -\langle \mathcal{O} K_\rho(R) \rangle_{\rho, \text{conn}}, \quad (\text{J6})$$

with $\langle \mathcal{O} \rangle_n \equiv \text{Tr}(\rho_{B_R}^n \mathcal{O}) / \text{Tr}(\rho_{B_R}^n)$.

Appendix K: Lattice implementation

In practice, lattice entanglement calculations are performed for integer Rényi index $n \geq 2$ via replica ratios [18]. Define

$$S_n(B_R; \rho) \equiv \frac{1}{1-n} \ln \text{Tr}(\rho_{B_R}^n), \quad n \in \mathbb{Z}_{\geq 2}. \quad (\text{K1})$$

For a fixed polarization λ define the vacuum-subtracted Rényi entropy and its radius flow,

$$\begin{aligned} \Delta S_n(B_R; h, \lambda) &\equiv S_n(B_R; \rho_{h, \lambda}) - S_n(B_R; \rho_0), \\ \mathfrak{s}_n(R; h, \lambda) &\equiv R \frac{d}{dR} \Delta S_n(B_R; h, \lambda). \end{aligned} \quad (\text{K2})$$

Unpolarized results are obtained by averaging the *flow* over λ ,

$$\mathfrak{s}_n(R; h) \equiv \frac{1}{2S+1} \sum_{\lambda=-S}^S \mathfrak{s}_n(R; h, \lambda). \quad (\text{K3})$$

1. Primary protocol

A practical lattice route proceeds as follows:

1. Prepare the hadron rest-frame state with a fixed spin/polarization projection using source/sink operators at $\tau_i < 0 < \tau_f$ with momentum projection $\mathbf{p}_0 = \mathbf{0}$, as in Eqs. (10) and (12).
2. Compute $S_n(B_R; \rho)$ for $\rho = \rho_{h, \lambda}$ and $\rho = \rho_0$ using replica ratios on an n -sheeted cut geometry with the same fixed replica prescription.
3. Form $\Delta S_n(B_R; h, \lambda)$ and, if desired, analytically continue (or extrapolate) $n \rightarrow 1$ to obtain $\Delta S_{\text{EE}}(B_R; h, \lambda)$.
4. Evaluate the radius-flow observable by a discrete derivative,

$$\mathfrak{s}_n(R; h, \lambda) \approx R \frac{\Delta S_n(B_{R+\delta R}; h, \lambda) - \Delta S_n(B_R; h, \lambda)}{\delta R}, \quad (\text{K4})$$

or by differentiating a correlated smooth fit to $\Delta S_n(R)$.

5. Average $\mathfrak{s}_n(R; h, \lambda)$ over λ to obtain unpolarized flows.
6. On candidate windows, fit the data to the mixed basis Eqs. (38) and (39), test the nested pure-endpoint limits, and optionally compare the fitted coefficient ratio with the holographic benchmark Eq. (52).

2. Minimal first lattice test

A first, low-overhead test is: (i) work at $n = 2$, (ii) use at least two spatial volumes at fixed lattice spacing and pion mass, scanning R over $a \ll R \ll L/2$, (iii) average over ball centers and cubic rotations to reduce cut discretization artifacts, (iv) form $\mathfrak{s}_2(R)$ from correlated fits to $\Delta S_2(R)$ and perform polarization averaging at the flow level; because replica-ratio estimators are noisy and discrete derivatives amplify correlations, a practical implementation should obtain $\mathfrak{s}_2(R)$ from a correlated smooth fit to $\Delta S_2(R)$ (or from correlated finite differences with controlled covariance), rather than from pointwise differencing; and (v) fit locally first to the pure endpoints and then to the mixed two-basis model.

The minimal reporting output is: (a) whether a boundary-dominated window exists, (b) the presence or absence of a pronounced intermediate- R extremum, (c) the extracted turning point and whether it is closer to $R_{\text{EE}}^{(0)}$ or $R_{\text{EE}}^{(2)}$, (d) the sign of the slope on either side of the extremum, (e) whether a second basis coefficient is statistically required, and (f) the stability of the preferred endpoint/mixed classification under lattice spacing, volume, and cut-discretization changes.

3. Excited-state contamination

Unless the source-sink separation $|\tau_f - \tau_i|$ is sufficiently large, excited-state contamination can distort the measured R dependence of $\Delta S_n(B_R; h, \lambda)$ and therefore of

the flow $\mathfrak{s}_n(R)$, potentially shifting or broadening the extracted turning point. Accordingly, the same stability checks used in standard lattice two- and three-point analyses should be performed here: vary $|\tau_f - \tau_i|$ (and/or use multistate fits) and require that the inferred window stability, endpoint preference, and mixed-fit coefficient ratio are stable within uncertainties.

Appendix L: Holographic derivation of the momentum-space hadron central charge

Unlike the Euclidean discussion in the main text, this appendix is written in Minkowski signature with the mostly-minus convention

$$\eta_{\mu\nu} = \text{diag}(+, -, -, -), \quad \mu, \nu = 0, 1, 2, 3. \quad (\text{L1})$$

The purpose of this appendix is to show, within a soft-wall AdS/QCD model, why the pole-subtracted integrated mixed stress-tensor correlator closes on the two-function basis $\{A(t), A^S(t)\}$ and why the benchmark combination quoted in the main text takes the form

$$\mathfrak{c}_h(t; p_0, m_0) \propto \left(1 - \frac{1}{3} \frac{m_0^2}{p_0^2}\right) A(t) - \frac{9}{32} \frac{m_0^2}{p_0^2} A^S(t). \quad (\text{L2})$$

The derivation is for a scalar target. Its role in the main text is limited: it motivates the mixed basis $\{A, A^S\}$ and supplies a model-dependent benchmark ratio inside that basis; it is *not* a first-principles nucleon derivation.

We start from the reduced four-point amplitude

$$\langle O_h(p_2) T(q_1) T^{00}(q_2) O_h(p_1) \rangle = (2\pi)^4 \delta^{(4)}(p_1 + q_1 - p_2 - q_2) \mathcal{M}_{T00}(p_2, q_2; p_1, q_1), \quad (\text{L3})$$

where $T \equiv T^\mu{}_\mu$. The exact spacetime integration of the first insertion imposes

$$q_1 = 0. \quad (\text{L4})$$

In that kinematics the uncontracted amplitude still contains the standard elastic external-line poles in the s - and u -channels. The finite object is therefore the *pole-subtracted* integrated correlator. We write

$$\boxed{\widetilde{\mathcal{M}}_{T00}^{\text{reg}}(q_2) \equiv \widetilde{\mathcal{M}}_{T00}^{\text{reg,exact}}(q_2) - \widetilde{\mathcal{M}}_{T00}^{(\text{ct})}(q_2)}, \quad (\text{L5})$$

where $\widetilde{\mathcal{M}}_{T00}^{\text{reg,exact}}$ is the exact pole-subtracted integrated correlator and $\widetilde{\mathcal{M}}_{T00}^{(\text{ct})}$ is the purely local two-graviton matter seagull. The quantity that carries the nonlocal GFF information is $\widetilde{\mathcal{M}}_{T00}^{\text{reg}}$, not $\widetilde{\mathcal{M}}_{T00}^{(\text{ct})}$.

The main result is obtained in exact integrated Breit kinematics,

$$q_1 = 0, \quad q_{2,0} = 0, \quad t \equiv q_2^2 = -Q_2^2 < 0, \quad (\text{L6})$$

and in the window

$$\kappa^2 \ll Q_2^2 \ll 4m_0^2. \quad (\text{L7})$$

There one finds

$$\boxed{\widetilde{\mathcal{M}}_{T00}^{\text{reg}}(q_2) \approx 2 \left[p_0^2 - \frac{1}{3} m_0^2 \right] \frac{1}{2\kappa_5^2} A(t) - \left(\frac{3}{2} m_0^2 \right) \frac{3}{16\kappa_5^2} A^S(t), \quad t = q_2^2}, \quad (\text{L8})$$

or, equivalently,

$$\widetilde{\mathcal{M}}_{T00}^{\text{reg}}(q_2) \approx 2p_0^2 \mathfrak{c}_h(t; p_0, m_0), \quad (\text{L9})$$

with

$$\mathbf{c}_h(t; p_0, m_0) = \frac{1}{2\kappa_5^2} \left[\left(1 - \frac{1}{3} \frac{m_0^2}{p_0^2} \right) A(t) - \frac{9}{32} \frac{m_0^2}{p_0^2} A^S(t) \right]. \quad (\text{L10})$$

The logic is straightforward: (i) decompose the four-point function into Witten-diagram channels; (ii) subtract the elastic scalar pole from the s - and u -channels; (iii) use the exact integrated projection $q_1 = 0$ to show that those pole-subtracted s - and u -channels vanish identically; (iv) identify the surviving nonlocal t -channel TT and spin-0 exchanges with the same spectral data that define $A(t)$ and $A^S(t)$; and (v) evaluate the resulting kinematic coefficients.

1. Soft-wall ingredients and form-factor definitions

We work on AdS₅ in Poincaré coordinates with

$$ds^2 = \bar{g}_{MN} dX^M dX^N = \frac{R^2}{z^2} (\eta_{\mu\nu} dx^\mu dx^\nu - dz^2), \quad z \in (0, \infty), \quad (\text{L11})$$

and soft-wall dilaton profile

$$\varphi(z) = \kappa^2 z^2. \quad (\text{L12})$$

For the present argument we only need three ingredients: the hadron ground-state wavefunction $\Phi_0(z)$, the non-normalizable TT profile $H(t, z)$, and the non-normalizable trace/scalar profile $F(t, z)$.

The scalar hadron is represented by a charged bulk field X dual to a boundary operator of dimension Δ_h , with ground-state mode

$$\Phi_0(z) = \mathcal{N}_0 z^{\Delta_h}, \quad m_0^2 = 2\kappa^2 \Delta_h, \quad \mathcal{N}_0^2 = \frac{2\kappa^2 \Delta_h^{-2}}{R^3 \Gamma(\Delta_h - 1)}. \quad (\text{L13})$$

The universal soft-wall measure appearing in the overlap integrals is

$$\mathcal{W}_2(z) = \frac{R^3}{z^3} e^{-\kappa^2 z^2}. \quad (\text{L14})$$

The TT and trace source profiles are normalized by

$$H(t, 0) = 1, \quad F(t, 0) = 1. \quad (\text{L15})$$

The corresponding three-point form factors are

$$F_h^{(2)}(t) \equiv \int_0^\infty dz \mathcal{W}_2(z) \Phi_0(z)^2 H(t, z), \quad F_h^{(0)}(t) \equiv \int_0^\infty dz \mathcal{W}_2(z) \Phi_0(z)^2 F(t, z). \quad (\text{L16})$$

In the scalar-target soft-wall model these are identified with the spin-2 and scalar/trace GFFs,

$$F_h^{(2)}(t) \equiv A(t), \quad F_h^{(0)}(t) \equiv A^S(t). \quad (\text{L17})$$

2. Channel decomposition, pole subtraction, and the exact $q_1 = 0$ selection

The full reduced amplitude decomposes as

$$\mathcal{M}_{T00} = \mathcal{M}_{T00}^{(s)} + \mathcal{M}_{T00}^{(u)} + \mathcal{M}_{T00}^{(ct)} + \mathcal{M}_{T00}^{(t,TT)} + \mathcal{M}_{T00}^{(t,0)}, \quad (\text{L18})$$

corresponding to the diagram classes shown in Fig. 10.

Let $G_X(z, z'; s)$ denote the scalar bulk-to-bulk propagator. The pole-subtracted version is obtained by removing the elastic $n = 0$ mode,

$$G_X^{\text{sub}}(z, z'; s) = \sum_{n \geq 1} \frac{\Phi_n(z) \Phi_n(z')}{s - m_n^2 + i\epsilon}. \quad (\text{L19})$$

The relevant source overlaps are

$$\mathcal{A}_{mn}(t) \equiv \int_0^\infty dz \mathcal{W}_2(z) \Phi_m(z) \Phi_n(z) H(t, z), \quad (\text{L20})$$

and

$$\mathcal{S}_{mn}(t) \equiv \int_0^\infty dz \mathcal{W}_2(z) \Phi_m(z) \Phi_n(z) F(t, z). \quad (\text{L21})$$

Because the integrated trace insertion is a zero-momentum Weyl source, the exact $q_1 = 0$ projection implies

$$F(0, z) = 1 \quad \implies \quad \mathcal{S}_{mn}(0) = \delta_{mn}. \quad (\text{L22})$$

This is the key simplification: the exact integrated source selects the elastic mode only. Since G_X^{sub} starts at $n = 1$, the pole-subtracted integrated s - and u -channel amplitudes vanish identically,

$$\boxed{\widetilde{\mathcal{M}}_{T00}^{(s,\text{sub})}(q_2) = 0, \quad \widetilde{\mathcal{M}}_{T00}^{(u,\text{sub})}(q_2) = 0.} \quad (\text{L23})$$

Therefore the exact pole-subtracted integrated correlator contains only a local contact term plus the nonlocal TT and spin-0 t -channel exchanges:

$$\widetilde{\mathcal{M}}_{T00}^{\text{reg,exact}}(q_2) = \widetilde{\mathcal{M}}_{T00}^{(\text{ct})}(q_2) + \widetilde{\mathcal{M}}_{T00}^{(t,TT)}(q_2) + \widetilde{\mathcal{M}}_{T00}^{(t,0)}(q_2), \quad (\text{L24})$$

so that

$$\boxed{\widetilde{\mathcal{M}}_{T00}^{\text{reg}}(q_2) = \widetilde{\mathcal{M}}_{T00}^{(t,TT)}(q_2) + \widetilde{\mathcal{M}}_{T00}^{(t,0)}(q_2).} \quad (\text{L25})$$

There is a second exact simplification specific to the integrated kinematics. For an even-spin TT exchange with $j \geq 4$, every extra top momentum is proportional to

$$q = \frac{q_2}{2} = -\frac{\Delta}{2}, \quad (\text{L26})$$

and is therefore annihilated by TT transversality. Hence

$$\boxed{\widetilde{\mathcal{M}}_{T00}^{(t,j,TT)}(q_2) \Big|_{q_1=0} = 0, \quad j = 4, 6, 8, \dots} \quad (\text{L27})$$

The exact integrated TT sector is therefore a pure spin-2 selector.

3. UV factorization onto the A and A^S channels

In the UV-dominated regime the reduced top vertices factorize onto the same spectral sums that appear in the three-point functions, so the nonlocal regular amplitude may be written as

$$\boxed{\widetilde{\mathcal{M}}_{T00}^{\text{reg}}(q_2) = \mathcal{K}_2(q_2, p) \widehat{\mathcal{C}}_T(t) A(t) + \mathcal{K}_0(q_2, p) \widehat{\mathcal{C}}_0(t) A^S(t), \quad t = q_2^2.} \quad (\text{L28})$$

Here \mathcal{K}_2 and \mathcal{K}_0 are purely kinematic factors, while $\widehat{\mathcal{C}}_T$ and $\widehat{\mathcal{C}}_0$ depend only on the chosen soft-wall completion.

For the minimal completion used in the main text, analytic continuation to spacelike momentum transfer,

$$t = -Q_2^2, \quad Q_2^2 > 0, \quad a_2 \equiv \frac{Q_2^2}{4\kappa^2}, \quad (\text{L29})$$

gives

$$\boxed{\widehat{\mathcal{C}}_T(-Q_2^2) = \frac{a_2}{2\kappa_5^2(a_2 + 2)} = \frac{Q_2^2}{2\kappa_5^2(Q_2^2 + 8\kappa^2)},} \quad (\text{L30})$$

and

$$\widehat{\mathcal{C}}_0(-Q_2^2) = \frac{3a_2}{16\kappa_5^2(a_2 + 2)} = \frac{3Q_2^2}{16\kappa_5^2(Q_2^2 + 8\kappa^2)}. \quad (\text{L31})$$

Hence, for $Q_2^2 \gg \kappa^2$,

$$\widehat{\mathcal{C}}_T(-Q_2^2) \approx \frac{1}{2\kappa_5^2}, \quad \widehat{\mathcal{C}}_0(-Q_2^2) \approx \frac{3}{16\kappa_5^2}. \quad (\text{L32})$$

4. Kinematics and the surviving coefficients

We use

$$p \equiv \frac{p_1 + p_2}{2}, \quad q \equiv \frac{q_1 + q_2}{2}, \quad \Delta \equiv p_2 - p_1 = q_1 - q_2, \quad t \equiv \Delta^2. \quad (\text{L33})$$

For equal-mass on-shell external states,

$$p_1^2 = p_2^2 = m_0^2, \quad p \cdot \Delta = 0, \quad 4p^2 = 4m_0^2 - t. \quad (\text{L34})$$

Under the exact integrated projection,

$$q_1 = 0, \quad q = \frac{q_2}{2}, \quad \Delta = -q_2, \quad t = q_2^2. \quad (\text{L35})$$

The TT projector is

$$\Pi_{\mu\nu,\alpha\beta}^{TT}(\Delta) = \frac{1}{2}(\theta_{\mu\alpha}\theta_{\nu\beta} + \theta_{\mu\beta}\theta_{\nu\alpha}) - \frac{1}{3}\theta_{\mu\nu}\theta_{\alpha\beta}, \quad \theta_{\mu\nu}(\Delta) = \eta_{\mu\nu} - \frac{\Delta_\mu\Delta_\nu}{\Delta^2}. \quad (\text{L36})$$

Contracting it with the scalar-target tensor structure gives the exact TT kinematic factor

$$\mathcal{K}_2(q_2, p) = 2 \left[\left(p_0 - \frac{\Delta_0(\Delta \cdot p)}{t} \right)^2 - \frac{1}{3} \left(1 - \frac{\Delta_0^2}{t} \right) \left(p^2 - \frac{(\Delta \cdot p)^2}{t} \right) \right]. \quad (\text{L37})$$

In the exact integrated kinematics $\Delta \cdot p = 0$, so

$$\mathcal{K}_2(q_2, p) = 2 \left[p_0^2 - \frac{1}{3} \left(1 - \frac{q_{2,0}^2}{q_2^2} \right) p^2 \right]. \quad (\text{L38})$$

In Breit kinematics $q_{2,0} = 0$ this reduces to

$$\mathcal{K}_2^{\text{Breit}}(q_2, p) = 2 \left[p_0^2 - \frac{1}{3} p^2 \right] = 2 \left[p_0^2 - \frac{1}{3} m_0^2 + \frac{t}{12} \right]. \quad (\text{L39})$$

The scalar/trace channel has a simpler role in the final benchmark. After the same exact $q_1 = 0$ projection and on-shell reduction, its leading small- $|t|$ prefactor is

$$\mathcal{K}_0(q_2, p) = -\frac{3}{2} m_0^2 + \mathcal{O}(t). \quad (\text{L40})$$

We do not display the full $\mathcal{O}(t)$ correction because it is not needed in the matching window Eq. (L7); the benchmark ratio follows entirely from the leading term.

Combining Eqs. (L28), (L32), (L39) and (L40) and dropping terms suppressed by $|t|/m_0^2$ gives

$$\widetilde{\mathcal{M}}_{T00}^{\text{reg}}(q_2) \approx 2 \left[p_0^2 - \frac{1}{3} m_0^2 \right] \frac{1}{2\kappa_5^2} A(t) - \left(\frac{3}{2} m_0^2 \right) \frac{3}{16\kappa_5^2} A^S(t), \quad t = q_2^2. \quad (\text{L41})$$

This is the nonlocal integrated trace-energy correlator formula used in the main text.

What is exact and what is asymptotic. It is useful to separate the logic into three layers:

1. *Exact after pole subtraction:* the integrated pole-subtracted correlator contains only the local seagull plus the TT and spin-0 t -channel exchanges, Eqs. (L24) and (L25).
2. *Exact after the $q_1 = 0$ projection:* the pole-subtracted s - and u -channels vanish identically, Eq. (L23), and higher even TT spins also drop out, Eq. (L27).
3. *Asymptotic in the window $\kappa^2 \ll Q_2^2 \ll 4m_0^2$:* the coefficient functions freeze to constants and the $\mathcal{O}(t/m_0^2)$ terms may be dropped, yielding Eq. (L41).

5. Momentum-space hadron central charge

Factoring out $2p_0^2$ defines the momentum-space hadron central charge,

$$\widetilde{\mathcal{M}}_{T00}^{\text{reg}}(q_2) \approx 2p_0^2 \mathbf{c}_h(t; p_0, m_0), \quad (\text{L42})$$

with

$$\mathbf{c}_h(t; p_0, m_0) = \frac{1}{2\kappa_5^2} \left[\left(1 - \frac{1}{3} \frac{m_0^2}{p_0^2} \right) A(t) - \frac{9}{32} \frac{m_0^2}{p_0^2} A^S(t) \right]. \quad (\text{L43})$$

Using the standard holographic normalization

$$2\kappa_5^2 = 16\pi G_N = \frac{8\pi^2}{N_c^2}, \quad \frac{1}{2\kappa_5^2} = \frac{N_c^2}{8\pi^2}, \quad (\text{L44})$$

this becomes

$$\mathbf{c}_h(t; p_0, m_0) = \frac{N_c^2}{8\pi^2} \left[\left(1 - \frac{1}{3} \frac{m_0^2}{p_0^2} \right) A(t) - \frac{9}{32} \frac{m_0^2}{p_0^2} A^S(t) \right]. \quad (\text{L45})$$

For separate partonic sectors $i \in \{q, g\}$ the same argument gives

$$\mathbf{c}_{h,i}(t; p_0, m_0) \propto \left[\left(1 - \frac{1}{3} \frac{m_0^2}{p_0^2} \right) A_i(t) - \frac{9}{32} \frac{m_0^2}{p_0^2} A_i^S(t) \right]. \quad (\text{L46})$$

This is the sector-decomposed relation quoted in the main text.

The derivation above was performed for a scalar target, so the nucleon use of the result should be read only as a basis-selection argument and a benchmark-ratio extrapolation. With that caveat, one makes the replacements

$$m_0 \rightarrow M_h, \quad p_0 \rightarrow E_h, \quad A(t) \rightarrow A_h(t), \quad A^S(t) \rightarrow A_h^S(t), \quad (\text{L47})$$

to obtain

$$\mathbf{c}_{h,i}(t; E_h, M_h) \propto \left[\left(1 - \frac{1}{3} \frac{M_h^2}{E_h^2} \right) A_i(t) - \frac{9}{32} \frac{M_h^2}{E_h^2} A_i^S(t) \right]. \quad (\text{L48})$$

The large-energy limit is then

$$\mathbf{c}_{h,i}(t; E_h \rightarrow \infty, M_h) \propto A_i(t). \quad (\text{L49})$$

Thus the integrated holographic response becomes spin-2 dominated at large energy, while the scalar/trace contribution is suppressed by M_h^2/E_h^2 .

Summary. Within the soft-wall model, the exact integrated projection $q_1 = 0$ kills the pole-subtracted s - and u -channels, leaving only TT and spin-0 t -channel exchange. Those two channels are precisely the ones that define the GFFs $A(t)$ and $A^S(t)$, so the nonlocal regular correlator closes on the two-function basis $\{A, A^S\}$. After evaluating the mostly-minus kinematics and taking the window $\kappa^2 \ll Q_2^2 \ll 4m_0^2$, one arrives at the benchmark combination Eq. (L43). This is the sole input from the holographic appendix used in the main text: it motivates the mixed basis and supplies a model-dependent ratio inside that basis, while the actual lattice analysis leaves the two coefficients free.

Appendix M: More details in the holographic calculation

In this appendix, we spell out the intermediate steps behind App. L. In particular, we show in detail why the exact integrated mixed stress-tensor correlator closes on the two-function basis $\{A(t), A^S(t)\}$ and why, in the soft-wall model, the nonlocal regular part takes the form stated in Eqs. (L41) and (L43).

We begin from the reduced four-point amplitude

$$\langle O_h(p_2) T(q_1) T^{00}(q_2) O_h(p_1) \rangle = (2\pi)^4 \delta^{(4)}(p_1 + q_1 - p_2 - q_2) \mathcal{M}_{T00}(p_2, q_2; p_1, q_1), \quad (\text{M1})$$

where $T \equiv T^\mu{}_\mu$. Exact spacetime integration of the first insertion imposes

$$q_1 = 0. \quad (\text{M2})$$

In that kinematics the uncontracted tensor amplitude still contains the standard elastic external-line poles in the s - and u -channels, so the physically relevant quantity is the *pole-subtracted* integrated correlator. We denote the exact pole-subtracted integrated correlator by $\widetilde{\mathcal{M}}_{T00}^{\text{reg,exact}}(q_2)$, including the purely local matter seagull, and define its nonlocal regular part by

$$\boxed{\widetilde{\mathcal{M}}_{T00}^{\text{reg}}(q_2) \equiv \widetilde{\mathcal{M}}_{T00}^{\text{reg,exact}}(q_2) - \widetilde{\mathcal{M}}_{T00}^{(\text{ct})}(q_2)}. \quad (\text{M3})$$

The model-dependent benchmark used in the main text concerns $\widetilde{\mathcal{M}}_{T00}^{\text{reg}}$, not the local seagull $\widetilde{\mathcal{M}}_{T00}^{(\text{ct})}$.

The detailed derivation below leads to the same asymptotic relation quoted in App. L. In exact integrated Breit kinematics,

$$q_1 = 0, \quad q_{2,0} = 0, \quad t \equiv q_2^2 = -Q_2^2 < 0, \quad (\text{M4})$$

and in the window

$$\kappa^2 \ll Q_2^2 \ll 4m_0^2, \quad Q_2^2 \equiv -q_2^2 > 0, \quad (\text{M5})$$

one finds

$$\boxed{\widetilde{\mathcal{M}}_{T00}^{\text{reg}}(q_2) \approx 2 \left[p_0^2 - \frac{1}{3} m_0^2 \right] \frac{1}{2\kappa_5^2} A(t) - \left(\frac{3}{2} m_0^2 \right) \frac{3}{16\kappa_5^2} A^S(t), \quad t = q_2^2.} \quad (\text{M6})$$

Equivalently,

$$\widetilde{\mathcal{M}}_{T00}^{\text{reg}}(q_2) \approx 2p_0^2 \mathbf{c}_h(t; p_0, m_0), \quad (\text{M7})$$

with

$$\boxed{\mathbf{c}_h(t; p_0, m_0) = \frac{1}{2\kappa_5^2} \left[\left(1 - \frac{1}{3} \frac{m_0^2}{p_0^2} \right) A(t) - \frac{9}{32} \frac{m_0^2}{p_0^2} A^S(t) \right].} \quad (\text{M8})$$

The derivation proceeds in five steps: (i) write the full Witten-diagram decomposition and define the pole-subtracted integrated amplitude; (ii) show that the exact $q_1 = 0$ projection annihilates the pole-subtracted s - and u -channels; (iii) derive the reduced top vertices from the effective 5D actions; (iv) factorize the surviving t -channel amplitudes into kinematic tensors times scalar spectral functions and identify those scalar functions with the hadronic GFFs; (v) evaluate the explicit kinematic contractions and the UV coefficient functions in the minimal soft-wall completion.

1. Five-dimensional effective description

We work on AdS₅ in Poincaré coordinates,

$$ds^2 = \bar{g}_{MN} dX^M dX^N = \frac{R^2}{z^2} (\eta_{\mu\nu} dx^\mu dx^\nu - dz^2), \quad z \in (0, \infty), \quad (\text{M9})$$

with soft-wall dilaton profile

$$\varphi(z) = \kappa^2 z^2. \quad (\text{M10})$$

The 5D description needed here is effective rather than microscopic:

$$S_{\text{eff}} = S_{\text{grav}} + S_X + S_X^{(2)} + S_{\text{bdy}} + S_{\text{gf}}. \quad (\text{M11})$$

The three relevant sectors are the TT graviton sector, the charged scalar hadron sector, and an effective spin-0 completion for the trace channel.

TT gravity sector. For the TT sector it is sufficient to use the standard soft-wall Einstein action in axial gauge as the effective generator of the TT equations,

$$S_{\text{grav}} = \frac{1}{2\kappa_5^2} \int d^5 X \sqrt{g} e^{-\varphi(z)} \left(\mathcal{R} + \frac{12}{R^2} \right) + \dots, \quad (\text{M12})$$

where the omitted terms are gauge-fixing and boundary pieces that do not affect the on-shell cubic vertices used below.

We parameterize the four-dimensional metric fluctuation by

$$g_{\mu\nu} = \frac{R^2}{z^2} \left(\eta_{\mu\nu} + h_{\mu\nu}^{TT} + \frac{1}{4} \eta_{\mu\nu} f + \dots \right), \quad h_{zM} = 0. \quad (\text{M13})$$

The omitted modes are longitudinal/vector fluctuations that do not contribute to the reduced exact $q_1 = 0$ amplitudes considered here.

The quadratic TT action may be written as [63]

$$S_{TT}^{(2)} = \frac{1}{8\kappa_5^2} \int d^4 x \int_0^\infty dz \mathcal{W}_2(z) \left[\partial_\rho h_{\mu\nu}^{TT} \partial^\rho h^{TT \mu\nu} + \partial_z h_{\mu\nu}^{TT} \partial_z h^{TT \mu\nu} \right], \quad (\text{M14})$$

with the standard soft-wall measure

$$\boxed{\mathcal{W}_2(z) = \frac{R^3}{z^3} e^{-\kappa^2 z^2}}. \quad (\text{M15})$$

Charged scalar hadron sector. The hadron is represented by a charged bulk scalar X dual to a boundary operator O_h of dimension Δ_h :

$$S_X = - \int d^5 X \sqrt{g} e^{-\varphi(z)} \left[g^{MN} \partial_M X^\dagger \partial_N X + m_5^2 |X|^2 \right], \quad m_5^2 R^2 = \Delta_h(\Delta_h - 4). \quad (\text{M16})$$

For a plane-wave mode $X(x, z) = e^{ip \cdot x} \Phi(z)$, the normalizable solutions are

$$\Phi_n(z) = \mathcal{N}_n z^{\Delta_h} L_n^{(\Delta_h-2)}(\kappa^2 z^2), \quad m_n^2 = 4\kappa^2 \left(n + \frac{\Delta_h}{2} \right), \quad (\text{M17})$$

with orthonormality

$$\int_0^\infty dz \mathcal{W}_2(z) \Phi_n(z) \Phi_m(z) = \delta_{nm}, \quad (\text{M18})$$

and normalization

$$\mathcal{N}_n = \sqrt{\frac{2\kappa^2 \Delta_h - 2}{R^3} \frac{n!}{\Gamma(n + \Delta_h - 1)}}. \quad (\text{M19})$$

The ground state is

$$\Phi_0(z) = \mathcal{N}_0 z^{\Delta_h}, \quad m_0^2 = 2\kappa^2 \Delta_h. \quad (\text{M20})$$

The scalar bulk-to-bulk propagator has the standard mode expansion

$$G_X(z, z'; s) = \sum_{n=0}^{\infty} \frac{\Phi_n(z) \Phi_n(z')}{s - m_n^2 + i\epsilon}. \quad (\text{M21})$$

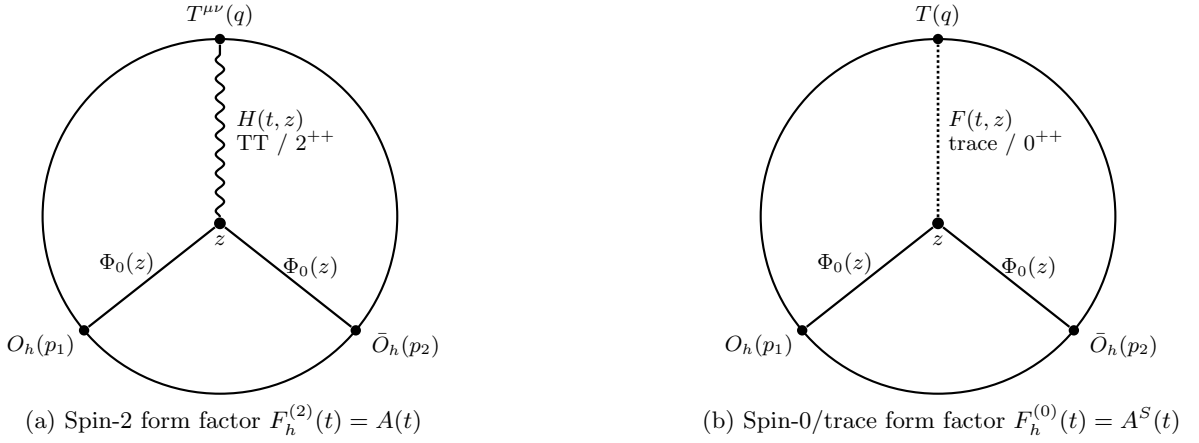


FIG. 12. **Three-point Witten diagrams for the charged-scalar-target gravitational form factors.** Panel (a) defines the spin-2 form factor $F_h^{(2)}(t)$ in Eq. (M36), with non-normalizable TT profile $H(t, z)$ normalized by Eq. (M35); in the scalar-target soft-wall model it is identified with $A(t)$ via Eq. (M37). Panel (b) defines the spin-0/trace form factor $F_h^{(0)}(t)$ in Eq. (M38), with non-normalizable trace profile $F(t, z)$ normalized by Eq. (M24); it is identified with $A^S(t)$ via Eq. (M39).

Effective spin-0 trace sector. Unlike the TT sector, the physical trace channel mixes the metric trace, longitudinal metric modes, and the dilaton. A complete diagonalization depends on the precise 5D Einstein-dilaton model. For the present correlator one only needs a normalizable spin-0 exchange and a non-normalizable trace source profile normalized to unity at the boundary, so we use the effective completion [63]

$$S_\chi^{(2)} = \frac{1}{4\kappa_5^2} \int d^4x \int_0^\infty dz \mathcal{W}_0(z) [\partial_\mu \chi \partial^\mu \chi + \partial_z \chi \partial_z \chi + U_0(z) \chi^2]. \quad (\text{M22})$$

The corresponding radial equation is

$$[-\mathcal{W}_0^{-1} \partial_z (\mathcal{W}_0 \partial_z) + U_0(z)] \psi(z) = t \psi(z), \quad (\text{M23})$$

with non-normalizable solution $F(t, z)$ normalized by

$$F(t, 0) = 1, \quad (\text{M24})$$

and normalizable modes $\Psi_\ell^{(0)}(z)$ satisfying

$$\int_0^\infty dz \mathcal{W}_0(z) \Psi_\ell^{(0)}(z) \Psi_{\ell'}^{(0)}(z) = \delta_{\ell\ell'}. \quad (\text{M25})$$

The scalar trace propagator is

$$G_0(z, z'; t) = \sum_{\ell=0}^{\infty} \frac{\Psi_\ell^{(0)}(z) \Psi_\ell^{(0)}(z')}{t - m_{0,\ell}^2 + i\epsilon}. \quad (\text{M26})$$

For explicit UV coefficient functions we later use the minimal soft-wall completion

$$\boxed{\mathcal{W}_0(z) = \mathcal{W}_2(z), \quad U_0(z) = 0.} \quad (\text{M27})$$

2. TT modes, source profiles, and the GFF building blocks

The TT radial equation is

$$\partial_z \left(\frac{e^{-\kappa^2 z^2}}{z^3} \partial_z \Psi^{(2)} \right) + \frac{e^{-\kappa^2 z^2}}{z^3} t \Psi^{(2)} = 0. \quad (\text{M28})$$

Its normalizable solutions are

$$\Psi_n^{(2)}(z) = \tilde{\mathcal{N}}_n z^4 L_n^{(2)}(\kappa^2 z^2), \quad m_{2,n}^2 = 4\kappa^2(n+2), \quad (\text{M29})$$

with orthonormality

$$\int_0^\infty dz \mathcal{W}_2(z) \Psi_n^{(2)}(z) \Psi_m^{(2)}(z) = \delta_{nm}, \quad (\text{M30})$$

and

$$\tilde{\mathcal{N}}_n = \sqrt{\frac{2\kappa^6}{R^3} \frac{n!}{\Gamma(n+3)}}. \quad (\text{M31})$$

The four-dimensional TT projector is

$$\Pi_{\mu\nu,\alpha\beta}^{TT}(\Delta) = \frac{1}{2} (\theta_{\mu\alpha}\theta_{\nu\beta} + \theta_{\mu\beta}\theta_{\nu\alpha}) - \frac{1}{3} \theta_{\mu\nu}\theta_{\alpha\beta}, \quad (\text{M32})$$

with

$$\theta_{\mu\nu}(\Delta) = \eta_{\mu\nu} - \frac{\Delta_\mu \Delta_\nu}{\Delta^2}. \quad (\text{M33})$$

The TT bulk-to-bulk propagator is

$$G_{\mu\nu,\alpha\beta}^{(2)}(z, z'; t) = \Pi_{\mu\nu,\alpha\beta}^{TT}(\Delta) \sum_{n=0}^{\infty} \frac{\Psi_n^{(2)}(z) \Psi_n^{(2)}(z')}{t - m_{2,n}^2 + i\epsilon}. \quad (\text{M34})$$

Let $H(t, z)$ denote the non-normalizable TT bulk-to-boundary profile normalized by

$$H(t, 0) = 1. \quad (\text{M35})$$

The corresponding spin-2 hadronic form factor is

$$F_h^{(2)}(t) \equiv \int_0^\infty dz \mathcal{W}_2(z) \Phi_0(z)^2 H(t, z). \quad (\text{M36})$$

In the scalar-target soft-wall model this is identified with the spin-2 GFF,

$$F_h^{(2)}(t) \equiv A(t), \quad (\text{M37})$$

see Fig. 12a.

Similarly, the non-normalizable spin-0/trace profile $F(t, z)$ defines

$$F_h^{(0)}(t) \equiv \int_0^\infty dz \mathcal{W}_2(z) \Phi_0(z)^2 F(t, z), \quad (\text{M38})$$

which we identify with the scalar/trace GFF,

$$F_h^{(0)}(t) \equiv A^S(t), \quad (\text{M39})$$

see Fig. 12b.

It is useful to make the corresponding spectral representation explicit. Introducing source residues $f_n^{(2)}$ and $f_\ell^{(0)}$ through the near-boundary expansion of the non-normalizable profiles, one may write

$$\begin{aligned} H(t, z) &= \sum_{n=0}^{\infty} \frac{f_n^{(2)} \Psi_n^{(2)}(z)}{t - m_{2,n}^2 + i\epsilon}, \\ F(t, z) &= \sum_{\ell=0}^{\infty} \frac{f_\ell^{(0)} \Psi_\ell^{(0)}(z)}{t - m_{0,\ell}^2 + i\epsilon}, \end{aligned} \quad (\text{M40})$$

so that the two form factors become

$$A(t) = \sum_{n=0}^{\infty} \frac{f_n^{(2)} g_n^{(2)}}{t - m_{2,n}^2 + i\epsilon}, \quad A^S(t) = \sum_{\ell=0}^{\infty} \frac{f_\ell^{(0)} g_\ell^{(0)}}{t - m_{0,\ell}^2 + i\epsilon}, \quad (\text{M41})$$

where the bottom overlaps $g_n^{(2)}$ and $g_\ell^{(0)}$ are defined below in Eq. (M57). These are precisely the spectral sums that reappear in the four-point function.

3. Kinematics

We use

$$p \equiv \frac{p_1 + p_2}{2}, \quad q \equiv \frac{q_1 + q_2}{2}, \quad \Delta \equiv p_2 - p_1 = q_1 - q_2, \quad t \equiv \Delta^2. \quad (\text{M42})$$

For equal-mass on-shell external states,

$$p_1^2 = p_2^2 = m_0^2, \quad p \cdot \Delta = 0, \quad 4p^2 = 4m_0^2 - t. \quad (\text{M43})$$

The exact integrated limit sets

$$q_1 = 0, \quad q = \frac{q_2}{2}, \quad \Delta = -q_2, \quad t = q_2^2. \quad (\text{M44})$$

For the final compact reduction we also choose exact integrated Breit kinematics,

$$q_{2,0} = 0. \quad (\text{M45})$$

4. Full Witten-diagram decomposition

The full reduced amplitude is the sum of s -, u -, local contact, and t -channel exchange diagrams:

$$\mathcal{M}_{T00} = \mathcal{M}_{T00}^{(s)} + \mathcal{M}_{T00}^{(u)} + \mathcal{M}_{T00}^{(ct)} + \mathcal{M}_{T00}^{(t,TT)} + \mathcal{M}_{T00}^{(t,0)}. \quad (\text{M46})$$

The diagrammatic content is the same as in Fig. 10: the first two terms are scalar s - and u -channel exchange, the third is the local two-graviton matter seagull, and the last two are the nonlocal TT and spin-0 t -channel exchanges.

5. Pole subtraction and exact disappearance of the integrated s - and u -channels

The key source overlaps are

$$\mathcal{A}_{mn}(t) \equiv \int_0^\infty dz \mathcal{W}_2(z) \Phi_m(z) \Phi_n(z) H(t, z), \quad (\text{M47})$$

and

$$\mathcal{S}_{mn}(t) \equiv \int_0^\infty dz \mathcal{W}_2(z) \Phi_m(z) \Phi_n(z) F(t, z). \quad (\text{M48})$$

Because the exactly integrated trace insertion is a zero-momentum Weyl rescaling, one has

$$F(0, z) = 1 \quad \implies \quad \mathcal{S}_{mn}(0) = \delta_{mn}. \quad (\text{M49})$$

This is the essential selection rule: the exact $q_1 = 0$ source projects onto the elastic mode only.

The un-subtracted s - and u -channel amplitudes contain the standard external-line elastic poles. The correct finite quantity is obtained by subtracting the elastic $n = 0$ pole from the exchanged scalar propagator,

$$G_X^{\text{sub}}(z, z'; s) = \sum_{n \geq 1} \frac{\Phi_n(z) \Phi_n(z')}{s - m_n^2 + i\epsilon}. \quad (\text{M50})$$

Then, in the exact integrated limit $q_1 = 0$, the source overlap Eq. (M49) selects the elastic mode $n = 0$, while the pole-subtracted propagator starts at $n = 1$. Therefore the pole-subtracted integrated s - and u -channel amplitudes vanish identically:

$$\boxed{\widetilde{\mathcal{M}}_{T00}^{(s,\text{sub})}(q_2) = 0, \quad \widetilde{\mathcal{M}}_{T00}^{(u,\text{sub})}(q_2) = 0.} \quad (\text{M51})$$

The statement is about the integrated amplitudes, not the kernel itself: $G_X^{\text{sub}}(z, z'; s)$ is nonzero, but its contraction with the exact $q_1 = 0$ source vanishes.

The exact pole-subtracted integrated correlator is therefore

$$\widetilde{\mathcal{M}}_{T00}^{\text{reg,exact}}(q_2) = \widetilde{\mathcal{M}}_{T00}^{(\text{ct})}(q_2) + \widetilde{\mathcal{M}}_{T00}^{(t,TT)}(q_2) + \widetilde{\mathcal{M}}_{T00}^{(t,0)}(q_2), \quad (\text{M52})$$

and hence

$$\boxed{\widetilde{\mathcal{M}}_{T00}^{\text{reg}}(q_2) = \widetilde{\mathcal{M}}_{T00}^{(t,TT)}(q_2) + \widetilde{\mathcal{M}}_{T00}^{(t,0)}(q_2).} \quad (\text{M53})$$

6. Bottom hadron vertices

For the elastic bottom vertices it is convenient to introduce the scalar-target tensor

$$\boxed{\mathbb{T}^{\alpha\beta}(p_2, p_1; m_0, m_0) = p_2^\alpha p_1^\beta + p_2^\beta p_1^\alpha - \eta^{\alpha\beta}(p_1 \cdot p_2 - m_0^2).} \quad (\text{M54})$$

The bottom couplings of the exchanged TT and spin-0 modes to the hadron are then

$$\mathcal{G}_n^{(2)\alpha\beta}(p_2, p_1) = g_n^{(2)} \mathbb{T}^{\alpha\beta}(p_2, p_1; m_0, m_0), \quad (\text{M55})$$

$$\mathcal{G}_\ell^{(0)}(p_2, p_1) = g_\ell^{(0)}, \quad (\text{M56})$$

with overlaps

$$g_n^{(2)} = \int_0^\infty dz \mathcal{W}_2(z) \Phi_0(z)^2 \Psi_n^{(2)}(z), \quad g_\ell^{(0)} = \int_0^\infty dz \mathcal{W}_2(z) \Phi_0(z)^2 \Psi_\ell^{(0)}(z). \quad (\text{M57})$$

The TT exchange carries the explicit tensor structure (M54); the scalar exchange is controlled by the traced scalar form factor and will be parameterized below by a reduced scalar invariant \mathcal{K}_0 after the exact integrated Breit projection.

7. Reduced $q_1 = 0$ top vertices from the effective actions

The exact integrated trace insertion acts as a zero-momentum Weyl source. In the reduced $q_1 = 0$ kinematics this source may be represented as

$$h_{\mu\nu}^{(1)}(x, z) = \frac{1}{4} \eta_{\mu\nu} f(x, z), \quad f(q_1 = 0, z) = F(0, z) = 1. \quad (\text{M58})$$

This observation makes it possible to obtain the relevant top cubic vertices by varying the quadratic 5D actions once with respect to that Weyl source.

TT top vertex. Varying the quadratic TT action Eq. (M14) by the zero-momentum Weyl source gives the reduced cubic interaction

$$\boxed{S_{fTT}^{(3)} = \frac{1}{8\kappa_5^2} \int d^4x \int_0^\infty dz \mathcal{W}_2(z) f(x, z) [\partial_\rho h_{\mu\nu}^{TT} \partial^\rho h^{TT\mu\nu} + \partial_z h_{\mu\nu}^{TT} \partial_z h^{TT\mu\nu}].} \quad (\text{M59})$$

Insert one external 00-source TT leg,

$$h_{\mu\nu}^{TT}(q_2, z) = \Pi_{\mu\nu,00}^{TT}(q_2) H(q_2, z) e^{iq_2 \cdot x}, \quad (\text{M60})$$

and one exchanged normalizable TT mode,

$$h_{\mu\nu}^{TT}(k, z) = \epsilon_{\mu\nu}^{TT}(k) \Psi_n^{(2)}(z) e^{ik \cdot x}, \quad k = -q_2. \quad (\text{M61})$$

Then the reduced top impact factor is

$$\mathcal{I}_n^{(2)\mu\nu}(q_2) \Big|_{q_1=0} = \frac{1}{4\kappa_5^2} \Pi^{TT\mu\nu}_{00}(q_2) J_n^{(T00)}(q_2^2), \quad (\text{M62})$$

with

$$J_n^{(T00)}(q_2^2) = \int_0^\infty dz \mathcal{W}_2(z) \left[q_2^2 H(q_2, z) \Psi_n^{(2)}(z) + \partial_z H(q_2, z) \partial_z \Psi_n^{(2)}(z) \right]. \quad (\text{M63})$$

Spin-0 top vertex. The corresponding reduced scalar interaction follows from the Weyl variation of the effective trace-sector action Eq. (M22):

$$S_{f\chi\chi}^{(3)} = \frac{1}{4\kappa_5^2} \int d^4x \int_0^\infty dz \mathcal{W}_0(z) f(x, z) \left[\frac{1}{4} \partial_\mu \chi \partial^\mu \chi + \frac{1}{2} \partial_z \chi \partial_z \chi + \frac{1}{2} U_0(z) \chi^2 \right]. \quad (\text{M64})$$

Define the trace projector

$$\Pi_{\mu\nu, \alpha\beta}^T \equiv \frac{1}{4} \eta_{\mu\nu} \eta_{\alpha\beta}, \quad \Pi^{T\mu\nu}_{00} = \frac{1}{4} \eta^{\mu\nu} \eta_{00}. \quad (\text{M65})$$

Then the reduced top scalar impact factor is

$$\mathcal{I}_\ell^{(0)\mu\nu}(q_2) \Big|_{q_1=0} = \Pi^{T\mu\nu}_{00} J_\ell^{(0;T00)}(q_2^2), \quad (\text{M66})$$

with

$$J_\ell^{(0;T00)}(q_2^2) = \int_0^\infty dz \mathcal{W}_0(z) \Psi_\ell^{(0)}(z) \left[\mathcal{K}_{fff}(q_2; \partial_z) F(q_2, z) + \mathcal{K}_{fTT}(q_2; \partial_z) H(q_2, z) \right]. \quad (\text{M67})$$

In the minimal scalar completion Eq. (M27) one may take

$$\mathcal{K}_{fff}(q; \partial_z) = \frac{1}{4\kappa_5^2} \left[\frac{1}{4} q^2 - \frac{1}{2} \mathcal{W}_0^{-1} \partial_z (\mathcal{W}_0 \partial_z) + \frac{1}{2} U_0(z) \right], \quad \mathcal{K}_{fTT}(q; \partial_z) = 0. \quad (\text{M68})$$

Hence, acting on the non-normalizable scalar profile,

$$\mathcal{K}_{fff}(q; \partial_z) F(q, z) = \frac{3}{16\kappa_5^2} q^2 F(q, z). \quad (\text{M69})$$

Local matter seagull. The local two-graviton matter contact term comes from the second variation of the scalar action Eq. (M16). Writing

$$g_{MN} = \bar{g}_{MN} + h_{MN}, \quad h \equiv \bar{g}^{MN} h_{MN}, \quad (\text{M70})$$

the standard expansions are

$$\sqrt{g} = \sqrt{\bar{g}} \left[1 + \frac{1}{2} h + \frac{1}{8} h^2 - \frac{1}{4} h_{MN} h^{MN} + \mathcal{O}(h^3) \right], \quad (\text{M71})$$

$$g^{MN} = \bar{g}^{MN} - h^{MN} + h^{MP} h_P^N + \mathcal{O}(h^3). \quad (\text{M72})$$

The cross term between two metric insertions $h^{(1)}$ and $h^{(2)}$ can be written as

$$S_X^{(2h)} = - \int d^5 X \sqrt{\bar{g}} e^{-\varphi} \left[B^{MN} [h^{(1)}, h^{(2)}] \partial_M X^\dagger \partial_N X + \frac{1}{2} \mathcal{C}_{\text{cross}} [h^{(1)}, h^{(2)}] (\bar{g}^{MN} \partial_M X^\dagger \partial_N X + m_5^2 |X|^2) \right], \quad (\text{M73})$$

where

$$B^{MN} [h^{(1)}, h^{(2)}] = h^{(1)MP} h^{(2)N}{}_{P} + h^{(2)MP} h^{(1)N}{}_{P} - \frac{1}{2} h^{(1)} h^{(2)MN} - \frac{1}{2} h^{(2)} h^{(1)MN}, \quad (\text{M74})$$

$$\mathcal{C}_{\text{cross}} [h^{(1)}, h^{(2)}] = \frac{1}{4} h^{(1)} h^{(2)} - \frac{1}{2} h_{PQ}^{(1)} h^{(2)PQ}. \quad (\text{M75})$$

For the polarizations relevant here,

$$h_{\mu\nu}^{(1)} = \frac{1}{4} \eta_{\mu\nu}, \quad h_{\mu\nu}^{(2)} = \epsilon_{\mu\nu}^{00} \mathcal{H}^{(00)}(q_2, z) e^{iq_2 \cdot x}, \quad (\text{M76})$$

the four-dimensional derivative seagull vanishes, while the radial-kinetic and mass cross terms survive. Evaluated on the hadron ground state, this gives

$$\widetilde{\mathcal{M}}_{T00}^{(\text{ct})}(q_2) = -\frac{1}{8} \int_0^\infty dz \mathcal{W}_2(z) \mathcal{H}^{(00)}(q_2, z) \left[\frac{z^2}{R^2} \Phi_0'(z)^2 + \frac{R^2}{z^2} m_5^2 \Phi_0(z)^2 \right]. \quad (\text{M77})$$

This term is purely local in the source and is not part of the nonlocal GFF result.

8. Exact t -channel factorization

The TT exchange amplitude is

$$\widetilde{\mathcal{M}}_{T00}^{(t,TT)}(q_2) = \sum_{n=0}^{\infty} \frac{\mathcal{I}_n^{(2)\mu\nu}(q_2)|_{q_1=0} \Pi_{\mu\nu\alpha\beta}^{TT}(q_2) \mathcal{G}_n^{(2)\alpha\beta}(p_2, p_1)}{q_2^2 - m_{2,n}^2 + i\epsilon}. \quad (\text{M78})$$

Substituting Eqs. (M55) and (M62) yields

$$\widetilde{\mathcal{M}}_{T00}^{(t,TT)}(q_2) = \mathcal{K}_2(q_2, p) \mathfrak{F}_{T00}^{(2)}(q_2^2), \quad (\text{M79})$$

with

$$\mathcal{K}_2(q_2, p) \equiv \Pi_{00,\alpha\beta}^{TT}(q_2) \mathbb{T}^{\alpha\beta}(p_2, p_1; m_0, m_0), \quad (\text{M80})$$

and

$$\mathfrak{F}_{T00}^{(2)}(q_2^2) = \frac{1}{4\kappa_5^2} \sum_{n=0}^{\infty} \frac{J_n^{(T00)}(q_2^2) g_n^{(2)}}{q_2^2 - m_{2,n}^2 + i\epsilon}. \quad (\text{M81})$$

For the scalar exchange the exact integrated $q_1 = 0$ amplitude takes the analogous form

$$\widetilde{\mathcal{M}}_{T00}^{(t,0)}(q_2) = \mathcal{K}_0(q_2, p) \mathfrak{F}_{T00}^{(0)}(q_2^2), \quad (\text{M82})$$

with

$$\mathfrak{F}_{T00}^{(0)}(q_2^2) = \sum_{\ell=0}^{\infty} \frac{J_\ell^{(0;T00)}(q_2^2) g_\ell^{(0)}}{q_2^2 - m_{0,\ell}^2 + i\epsilon}. \quad (\text{M83})$$

Here $\mathcal{K}_0(q_2, p)$ is the reduced scalar invariant generated by the effective spin-0 top vertex and the traced scalar hadron coupling. The exact covariant form depends on the normalization convention chosen for the effective spin-0

completion; the only form we actually need for the proof of App. L is its exact integrated Breit reduction, displayed below in Eq. (M110).

Therefore the exact nonlocal regular amplitude is already factorized:

$$\boxed{\widetilde{\mathcal{M}}_{T00}^{\text{reg}}(q_2) = \mathcal{K}_2(q_2, p) \mathfrak{F}_{T00}^{(2)}(q_2^2) + \mathcal{K}_0(q_2, p) \mathfrak{F}_{T00}^{(0)}(q_2^2)}. \quad (\text{M84})$$

In the UV-dominated regime the top overlaps factorize through the same source residues that appear in the form-factor spectral representations:

$$\mathcal{I}_n^{(2)\mu\nu}(q_2)|_{q_1=0} \xrightarrow{\text{UV}} \widehat{\mathcal{C}}_T(t) f_n^{(2)} \Pi^{TT\mu\nu}_{00}(q_2), \quad (\text{M85})$$

$$\mathcal{I}_\ell^{(0)\mu\nu}(q_2)|_{q_1=0} \xrightarrow{\text{UV}} \widehat{\mathcal{C}}_0(t) f_\ell^{(0)} \Pi^{T\mu\nu}_{00}. \quad (\text{M86})$$

Using Eq. (M41), one obtains the UV-factorized form

$$\boxed{\widetilde{\mathcal{M}}_{T00}^{\text{reg}}(q_2) \xrightarrow{\text{UV}} \mathcal{K}_2(q_2, p) \widehat{\mathcal{C}}_T(t) A(t) + \mathcal{K}_0(q_2, p) \widehat{\mathcal{C}}_0(t) A^S(t)}. \quad (\text{M87})$$

9. Explicit UV coefficient functions in the minimal soft-wall completion

To obtain explicit coefficient functions, analytically continue to Euclidean momentum transfer,

$$q_2^2 = -Q_2^2, \quad Q_2^2 > 0, \quad a_2 \equiv \frac{Q_2^2}{4\kappa^2}. \quad (\text{M88})$$

The final asymptotic relation is then read off after analytic continuation back to the physical Minkowski kinematics. Because the coefficient functions saturate to constants at large Q_2^2 , the leading window formula is insensitive to the continuation at the level used in the main text.

In the minimal completion Eq. (M27), the non-normalizable TT profile is

$$H(-Q_2^2, z) = \Gamma(a_2 + 2) U(a_2, -1, \kappa^2 z^2), \quad (\text{M89})$$

or equivalently

$$H(-Q_2^2, z) = a_2(a_2 + 1) \int_0^1 dx x^{a_2-1} (1-x) \exp\left[-\kappa^2 z^2 \frac{x}{1-x}\right]. \quad (\text{M90})$$

Its radial derivative is

$$\partial_z H(-Q_2^2, z) = -2\kappa^2 z a_2(a_2 + 1) \int_0^1 dx x^{a_2} \exp\left[-\kappa^2 z^2 \frac{x}{1-x}\right]. \quad (\text{M91})$$

Near the boundary,

$$\Psi_n^{(2)}(z) \sim c_n^{(2)} z^4, \quad c_n^{(2)} = \widetilde{\mathcal{N}}_n L_n^{(2)}(0) = \widetilde{\mathcal{N}}_n \frac{(n+1)(n+2)}{2}. \quad (\text{M92})$$

The TT source residues are therefore

$$f_n^{(2)} = -4R^3 c_n^{(2)}. \quad (\text{M93})$$

Using Eqs. (M90) and (M91) in Eq. (M63) gives the UV relation

$$J_n^{(T00)}(-Q_2^2) \xrightarrow{\text{UV}} -8R^3 c_n^{(2)} \frac{a_2}{a_2 + 2}. \quad (\text{M94})$$

Hence

$$\boxed{\widehat{\mathcal{C}}_T(-Q_2^2) = \frac{a_2}{2\kappa_5^2(a_2 + 2)} = \frac{Q_2^2}{2\kappa_5^2(Q_2^2 + 8\kappa^2)}}. \quad (\text{M95})$$

For the scalar sector, the minimal completion Eq. (M69) gives

$$\mathcal{K}_{fff}F = \frac{3}{16\kappa_5^2}q_2^2 F = -\frac{3Q_2^2}{16\kappa_5^2}F. \quad (\text{M96})$$

The same UV residue analysis then yields

$$\widehat{\mathcal{C}}_0(-Q_2^2) = \frac{3a_2}{16\kappa_5^2(a_2+2)} = \frac{3Q_2^2}{16\kappa_5^2(Q_2^2+8\kappa^2)}. \quad (\text{M97})$$

Therefore, in the UV regime $Q_2^2 \gg \kappa^2$,

$$\widehat{\mathcal{C}}_T(-Q_2^2) \approx \frac{1}{2\kappa_5^2}, \quad \widehat{\mathcal{C}}_0(-Q_2^2) \approx \frac{3}{16\kappa_5^2}. \quad (\text{M98})$$

In the same minimal completion, the 00-source profile entering the local seagull may be written as

$$\mathcal{H}^{(00)}(q_2, z) = \Pi_{00,00}^{TT}(q_2) H(q_2, z) + \frac{1}{4} F(q_2, z). \quad (\text{M99})$$

If one furthermore uses the minimal identification $F = H$, then

$$\mathcal{H}^{(00)}(q_2, z) = \Lambda_{00}(q_2) H(q_2, z), \quad \Lambda_{00}(q_2) = \Pi_{00,00}^{TT}(q_2) + \frac{1}{4}. \quad (\text{M100})$$

With

$$\Phi_0(z) = \mathcal{N}_0 z^{\Delta_h}, \quad \mathcal{N}_0^2 = \frac{2\kappa^{2\Delta_h-2}}{R^3 \Gamma(\Delta_h-1)}, \quad m_5^2 R^2 = \Delta_h(\Delta_h-4), \quad (\text{M101})$$

the local contact term Eq. (M77) can be written in closed form as

$$\widetilde{\mathcal{M}}_{T00}^{(\text{ct})}(q_2) = -\frac{\Lambda_{00}(q_2)}{8} \frac{\Gamma(a_2+2)\Gamma(\Delta_h+1)}{\Gamma(a_2+\Delta_h)} \left[\frac{\Delta_h^2}{R^2(a_2+\Delta_h)} + \kappa^2 \frac{\Delta_h-4}{\Delta_h-2} \right]. \quad (\text{M102})$$

Again, this local term is not part of the nonlocal GFF result, but may be added back whenever one wants $\widetilde{\mathcal{M}}_{T00}^{\text{reg,exact}}$ rather than $\widetilde{\mathcal{M}}_{T00}^{\text{reg}}$.

10. Exact TT contraction and exact integrated Breit reduction

Using

$$p_2 = p + \frac{\Delta}{2}, \quad p_1 = p - \frac{\Delta}{2}, \quad p_1 \cdot p_2 = p^2 - \frac{t}{4}, \quad (\text{M103})$$

the scalar-target tensor becomes

$$\mathbb{T}^{\alpha\beta}(p_2, p_1; m_0, m_0) = 2p^\alpha p^\beta - \frac{1}{2} \Delta^\alpha \Delta^\beta - \eta^{\alpha\beta} \left(p^2 - \frac{t}{4} - m_0^2 \right). \quad (\text{M104})$$

Because the TT projector is traceless and transverse,

$$\Pi_{\mu\nu,\alpha\beta}^{TT}(\Delta) \eta^{\alpha\beta} = 0, \quad \Pi_{\mu\nu,\alpha\beta}^{TT}(\Delta) \Delta^\alpha = 0, \quad (\text{M105})$$

only the $2p^\alpha p^\beta$ term survives in the TT contraction. A short calculation gives

$$\mathcal{K}_2(q_2, p) = 2 \left[\left(p_0 - \frac{\Delta_0(\Delta \cdot p)}{t} \right)^2 - \frac{1}{3} \left(1 - \frac{\Delta_0^2}{t} \right) \left(p^2 - \frac{(\Delta \cdot p)^2}{t} \right) \right]. \quad (\text{M106})$$

In the exact integrated equal-mass kinematics,

$$\Delta = -q_2, \quad p \cdot q_2 = 0, \quad (\text{M107})$$

so

$$\mathcal{K}_2(q_2, p) \Big|_{q_1=0} = 2 \left[p_0^2 - \frac{1}{3} \left(1 - \frac{q_{2,0}^2}{q_2^2} \right) p^2 \right]. \quad (\text{M108})$$

In exact integrated Breit kinematics, $q_{2,0} = 0$, this reduces to

$$\mathcal{K}_2^{\text{Breit}}(q_2, p) = 2 \left[p_0^2 - \frac{1}{3} p^2 \right] = 2 \left[p_0^2 - \frac{1}{3} m_0^2 + \frac{t}{12} \right]. \quad (\text{M109})$$

For the scalar channel, the exact covariant form of $\mathcal{K}_0(q_2, p)$ depends on the normalization convention used for the effective spin-0 completion. However, the only form needed in the proof of App. L is its exact integrated Breit reduction. Evaluating the scalar exchange generated by Eqs. (M64) and (M69) with one trace source and one T^{00} source gives

$$\mathcal{K}_0^{\text{Breit}}(q_2, p) = - \left(\frac{3}{2} m_0^2 + \frac{1}{4} q_2^2 \right) = - \left(\frac{3}{2} m_0^2 + \frac{1}{4} t \right). \quad (\text{M110})$$

This is the exact integrated Breit scalar invariant entering the final reduction. It is this quantity, rather than a separate pure-trace projector contraction, that controls the scalar exchange in the conventions used here.

Substituting Eqs. (M109) and (M110) into the UV-factorized amplitude Eq. (M87) yields the exact integrated Breit expression

$$\widetilde{\mathcal{M}}_{T00}^{\text{reg}}(q_2) = 2 \left[p_0^2 - \frac{1}{3} p^2 \right] \widehat{\mathcal{C}}_T(q_2^2) A(q_2^2) - \left(\frac{3}{2} m_0^2 + \frac{1}{4} q_2^2 \right) \widehat{\mathcal{C}}_0(q_2^2) A^S(q_2^2). \quad (\text{M111})$$

Using the on-shell identity $p^2 = m_0^2 - \frac{1}{4} q_2^2$, this becomes

$$\widetilde{\mathcal{M}}_{T00}^{\text{reg}}(q_2) = 2 \left[p_0^2 - \frac{1}{12} (4m_0^2 - q_2^2) \right] \widehat{\mathcal{C}}_T(q_2^2) A(q_2^2) - \left(\frac{3}{2} m_0^2 + \frac{1}{4} q_2^2 \right) \widehat{\mathcal{C}}_0(q_2^2) A^S(q_2^2). \quad (\text{M112})$$

Since $q_2^2 = t = -Q_2^2$, this may also be written as

$$\widetilde{\mathcal{M}}_{T00}^{\text{reg}}(q_2) = 2 \left[p_0^2 - \frac{1}{12} (4m_0^2 + Q_2^2) \right] \widehat{\mathcal{C}}_T(-Q_2^2) A(-Q_2^2) - \left(\frac{3}{2} m_0^2 - \frac{1}{4} Q_2^2 \right) \widehat{\mathcal{C}}_0(-Q_2^2) A^S(-Q_2^2). \quad (\text{M113})$$

11. Final reduction in the window $\kappa^2 \ll Q_2^2 \ll 4m_0^2$

Now impose the hierarchy

$$\kappa^2 \ll Q_2^2 \ll 4m_0^2, \quad q_2^2 = -Q_2^2. \quad (\text{M114})$$

In this regime the coefficient functions freeze to the constants in Eq. (M98), while the explicit q_2^2 corrections in Eq. (M112) are parametrically small compared with m_0^2 . Thus

$$2 \left[p_0^2 - \frac{1}{12} (4m_0^2 - q_2^2) \right] \approx 2 \left[p_0^2 - \frac{1}{3} m_0^2 \right], \quad (\text{M115})$$

and

$$\frac{3}{2} m_0^2 + \frac{1}{4} q_2^2 \approx \frac{3}{2} m_0^2. \quad (\text{M116})$$

Therefore

$$\boxed{\widetilde{\mathcal{M}}_{T00}^{\text{reg}}(q_2) \approx 2 \left[p_0^2 - \frac{1}{3} m_0^2 \right] \frac{1}{2\kappa_5^2} A(t) - \left(\frac{3}{2} m_0^2 \right) \frac{3}{16\kappa_5^2} A^S(t), \quad t = q_2^2.} \quad (\text{M117})$$

This is exactly the result quoted in App. L; compare Eq. (L41).

It is useful to separate three layers of the argument:

1. *Exact after pole subtraction*: the exact integrated pole-subtracted correlator is the sum of the local seagull and the TT/spin-0 t -channel exchanges, Eqs. (M52) and (M53).
2. *Exact after UV factorization*: the nonlocal regular amplitude closes on the basis $\{A(t), A^S(t)\}$, Eq. (M87).
3. *Asymptotic in the window $\kappa^2 \ll Q_2^2 \ll 4m_0^2$* : the coefficient functions freeze to constants and the explicit t/m_0^2 corrections may be dropped, yielding Eq. (M117).

12. Momentum-space hadron central charge

Factoring out $2p_0^2$ from Eq. (M117) defines the momentum-space hadron central charge,

$$\widetilde{\mathcal{M}}_{T00}^{\text{reg}}(q_2) \approx 2p_0^2 \mathbf{c}_h(t; p_0, m_0), \quad (\text{M118})$$

with

$$\boxed{\mathbf{c}_h(t; p_0, m_0) = \frac{1}{2\kappa_5^2} \left[\left(1 - \frac{1}{3} \frac{m_0^2}{p_0^2} \right) A(t) - \frac{9}{32} \frac{m_0^2}{p_0^2} A^S(t) \right].} \quad (\text{M119})$$

Using the standard holographic normalization

$$2\kappa_5^2 = 16\pi G_N = \frac{8\pi^2}{N_c^2}, \quad \frac{1}{2\kappa_5^2} = \frac{N_c^2}{8\pi^2}, \quad (\text{M120})$$

this becomes

$$\boxed{\mathbf{c}_h(t; p_0, m_0) = \frac{N_c^2}{8\pi^2} \left[\left(1 - \frac{1}{3} \frac{m_0^2}{p_0^2} \right) A(t) - \frac{9}{32} \frac{m_0^2}{p_0^2} A^S(t) \right].} \quad (\text{M121})$$

For separate partonic sectors $i \in \{q, g\}$ the same reasoning gives

$$\boxed{\mathbf{c}_{h,i}(t; p_0, m_0) \propto \left[\left(1 - \frac{1}{3} \frac{m_0^2}{p_0^2} \right) A_i(t) - \frac{9}{32} \frac{m_0^2}{p_0^2} A_i^S(t) \right].} \quad (\text{M122})$$

This is the sector-decomposed relation used in the main text.

Although the explicit derivation was carried out for a scalar target, the final answer depends only on the spin-2 and spin-0 hadronic GFFs. The step to the nucleon should therefore be read only as a basis-motivation and benchmark-ratio extrapolation. With that understanding, one makes the replacements

$$m_0 \rightarrow M_h, \quad p_0 \rightarrow E_h, \quad A(t) \rightarrow A_h(t), \quad A^S(t) \rightarrow A_h^S(t), \quad (\text{M123})$$

to obtain

$$\boxed{\mathbf{c}_{h,i}(t; E_h, M_h) \propto \left[\left(1 - \frac{1}{3} \frac{M_h^2}{E_h^2} \right) A_i(t) - \frac{9}{32} \frac{M_h^2}{E_h^2} A_i^S(t) \right].} \quad (\text{M124})$$

The large-energy limit is then

$$\boxed{\mathbf{c}_{h,i}(t; E_h \rightarrow \infty, M_h) \propto A_i(t).} \quad (\text{M125})$$

Thus the integrated holographic response becomes spin-2 dominated at large energy, while the scalar/trace contribution is suppressed by M_h^2/E_h^2 .

13. Exact spin-2 selection in the integrated TT sector

There is an additional structural simplification in the exact integrated kinematics. Consider a minimal Reggeized TT exchange of even spin j . The corresponding top tensor may be written schematically as

$$\mathcal{Q}_{00}^{(j)\mu_1\cdots\mu_j}(q, \Delta) = \text{ST}[\Pi^{TT\mu_1\mu_2}_{00}(\Delta) q^{\mu_3} \cdots q^{\mu_j}], \quad (\text{M126})$$

where ST denotes symmetrization and trace subtraction. In the exact integrated limit,

$$q = \frac{q_2}{2}, \quad \Delta = -q_2, \quad q = -\frac{\Delta}{2}. \quad (\text{M127})$$

Hence every extra factor of q is proportional to Δ , while the TT projector is transverse on every index. Therefore every even TT spin $j \geq 4$ is annihilated:

$$\boxed{\widetilde{\mathcal{M}}_{T00}^{(t,j,TT)}(q_2)\Big|_{q_1=0} = 0, \quad j = 4, 6, 8, \dots} \quad (\text{M128})$$

whereas $j = 2$ survives because there are no extra q -indices to kill. Thus the exact integrated TT sector is a pure spin-2 selector.

Summary. The detailed holographic picture is therefore:

1. the full mixed correlator decomposes into s -, u -, contact, and t -channel Witten diagrams;
2. the correct finite integrated quantity is the pole-subtracted correlator;
3. the exact $q_1 = 0$ projection annihilates the pole-subtracted s - and u -channels;
4. the remaining nonlocal regular amplitude is the sum of TT and spin-0 t -channel exchanges;
5. in the UV-dominated Breit window those exchanges reduce to the two hadronic GFFs $A(t)$ and $A^S(t)$ with the explicit coefficients in Eq. (M117);
6. the associated momentum-space hadron central charge is Eq. (M119), reproducing Eq. (L43).

This is the detailed holographic input behind the concise argument in App. L. Its only role in the main text is to motivate the mixed basis $\{A, A^S\}$ and to provide a model-dependent benchmark ratio inside that basis. The actual lattice analysis leaves the coefficients of A and A^S free.

- | | |
|--|---|
| <p>[1] L. Bombelli, R. K. Koul, J. Lee, and R. D. Sorkin, Phys. Rev. D 34, 373 (1986).</p> <p>[2] M. Srednicki, Phys. Rev. Lett. 71, 666 (1993).</p> <p>[3] C. G. Callan and F. Wilczek, Phys. Lett. B 333, 55 (1994), arXiv:hep-th/9401072 [hep-th].</p> <p>[4] P. Calabrese and J. Cardy, J. Stat. Mech. 2004, P06002 (2004), arXiv:hep-th/0405152 [hep-th].</p> <p>[5] S. Ryu and T. Takayanagi, Phys. Rev. Lett. 96, 181602 (2006), arXiv:hep-th/0603001 [hep-th].</p> <p>[6] S. Ryu and T. Takayanagi, JHEP 08, 045, arXiv:hep-th/0605073 [hep-th].</p> <p>[7] I. R. Klebanov, D. Kutasov, and A. Murugan, Nucl. Phys. B 796, 274 (2008), arXiv:0709.2140 [hep-th].</p> <p>[8] S. N. Solodukhin, Phys. Lett. B 665, 305 (2008), arXiv:0802.3117.</p> <p>[9] P. V. Buividovich and M. I. Polikarpov, Phys. Lett. B 670, 141 (2008), arXiv:0806.3376 [hep-th].</p> <p>[10] H. Casini, M. Huerta, and R. C. Myers, JHEP 05, 036,</p> | <p>arXiv:1102.0440 [hep-th].</p> <p>[11] H. Casini, M. Huerta, and J. A. Rosabal, Phys. Rev. D 89, 085012 (2014), arXiv:1312.1183 [hep-th].</p> <p>[12] V. Rosenhaus and M. Smolkin, JHEP 12, 179, arXiv:1403.3733 [hep-th].</p> <p>[13] V. Rosenhaus and M. Smolkin, Phys. Rev. Lett. 113, 261602 (2014), arXiv:1406.2716 [hep-th].</p> <p>[14] W. Donnelly and A. C. Wall, Phys. Rev. Lett. 114, 111603 (2015), arXiv:1412.1895 [hep-th].</p> <p>[15] O. Ben-Ami, I. Carmi, and M. Smolkin, JHEP 08, 048, arXiv:1504.00913 [hep-th].</p> <p>[16] R. M. Soni and S. P. Trivedi, JHEP 01, 136, arXiv:1510.07455 [hep-th].</p> <p>[17] T. Nishioka and T. Takayanagi, JHEP 01, 090, arXiv:hep-th/0611035.</p> <p>[18] P. V. Buividovich and M. I. Polikarpov, Nucl. Phys. B 802, 458 (2008), arXiv:0802.4247 [hep-lat].</p> <p>[19] A. Velytsky, PoS LATTICE2008, 256 (2008),</p> |
|--|---|

- arXiv:0809.4502 [hep-lat].
- [20] Y. Nakagawa, A. Nakamura, S. Motoki, and V. I. Zakharov, PoS **LAT2009**, 188 (2009), arXiv:0911.2596 [hep-lat].
- [21] Y. Nakagawa, A. Nakamura, S. Motoki, and V. I. Zakharov, PoS **LATTICE2010**, 281 (2010), arXiv:1104.1011 [hep-lat].
- [22] E. Itou, T. Nagata, Y. Nakagawa, A. Nakamura, and V. I. Zakharov, Prog. Theor. Exp. Phys. **2016**, 061B01 (2016), arXiv:1512.01334 [hep-th].
- [23] A. Rabenstein, N. Bodendorfer, P. Buividovich, and A. Schäfer, Phys. Rev. D **100**, 034504 (2019), arXiv:1812.04279 [hep-lat].
- [24] T. Rindlisbacher, N. Jokela, A. Pönni, K. Rummukainen, and A. Salami, PoS **LATTICE2022**, 031 (2022), arXiv:2211.00425 [hep-lat].
- [25] N. Jokela, A. Pönni, T. Rindlisbacher, K. Rummukainen, and A. Salami, JHEP **12**, 137, arXiv:2304.08949 [hep-th].
- [26] R. M. Soni and S. P. Trivedi, JHEP **01**, 136, arXiv:1510.07455 [hep-th].
- [27] A. Agarwal, D. Karabali, and V. P. Nair, Phys. Rev. D **96**, 125008 (2017), arXiv:1701.00014 [hep-th].
- [28] W. Donnelly, S. Timmerman, and N. Valdés-Meller, JHEP **04**, 182, arXiv:1911.09302 [hep-th].
- [29] T. Anegawa, N. Iizuka, and D. Kabat, Phys. Rev. D **105**, 085003 (2022), arXiv:2111.03886 [hep-th].
- [30] V. Panizza, R. C. de Almeida, and P. Hauke, JHEP **09**, 196, arXiv:2207.00605 [hep-th].
- [31] Y. Liu, M. A. Nowak, and I. Zahed, Phys. Rev. D **107**, 054010 (2023), arXiv:2205.06724 [hep-ph].
- [32] A. Bulgarelli and M. Panero, JHEP **06**, 030, arXiv:2304.03311 [quant-ph].
- [33] A. Freese and G. A. Miller, Phys. Rev. D **103**, 094023 (2021), arXiv:2102.01683 [hep-ph].
- [34] G. A. Miller, Phys. Rev. C **112**, 045204 (2025), arXiv:2507.14388 [hep-ph].
- [35] T. T. Takahashi and Y. Kanada-En'yo, Phys. Rev. D **100**, 114502 (2019), arXiv:1910.00859 [hep-lat].
- [36] T. T. Takahashi and Y. Kanada-En'yo, Phys. Rev. D **103**, 034504 (2021), arXiv:2011.10950 [hep-lat].
- [37] R. Amorosso, S. Syritsyn, and R. Venugopalan, Phys. Lett. B **868**, 139806 (2025), arXiv:2411.12818 [hep-lat].
- [38] R. Amorosso, S. Syritsyn, and R. Venugopalan, JHEP **12**, 177, arXiv:2410.00112 [hep-lat].
- [39] R. Amorosso, S. Syritsyn, and R. Venugopalan, PoS **LATTICE2024**, 409 (2025), arXiv:2502.08737 [hep-lat].
- [40] S. Grieninger, D. E. Kharzeev, and E. Marroquin, Phys. Rev. D **113**, 036013 (2026), arXiv:2510.23919 [hep-ph].
- [41] K. A. Mamo, Phys. Rev. D **112**, L111506 (2025), arXiv:2507.00176 [hep-ph].
- [42] S. N. Solodukhin, Living Rev. Rel. **14**, 8 (2011), arXiv:1104.3712 [hep-th].
- [43] H. Casini and M. Huerta, J. Phys. A **42**, 504007 (2009), arXiv:0905.2562 [hep-th].
- [44] P. Calabrese and J. Cardy, J. Phys. A **42**, 504005 (2009), arXiv:0905.4013 [cond-mat.stat-mech].
- [45] K.-W. Huang, Phys. Rev. D **92**, 025010 (2015), arXiv:1412.2730 [hep-th].
- [46] D. C. Hackett, D. A. Pefkou, and P. E. Shanahan, Phys. Rev. Lett. **132**, 251904 (2024), arXiv:2310.08484 [hep-lat].
- [47] J. J. Bisognano and E. H. Wichmann, J. Math. Phys. **17**, 303 (1976).
- [48] X. Ji, Phys. Rev. D **55**, 7114 (1997), arXiv:hep-ph/9609381 [hep-ph].
- [49] M. V. Polyakov and C. Weiss, Phys. Rev. D **60**, 114017 (1999), arXiv:hep-ph/9902451 [hep-ph].
- [50] M. V. Polyakov, Phys. Lett. B **555**, 57 (2003), arXiv:hep-ph/0210165.
- [51] B. Pasquini, M. V. Polyakov, and M. Vanderhaeghen, Phys. Lett. B **739**, 133 (2014), arXiv:1407.5960 [hep-ph].
- [52] V. D. Burkert, L. Elouadrhiri, and F. X. Girod, Nature **557**, 396 (2018).
- [53] M. V. Polyakov and P. Schweitzer, Eur. Phys. J. A **55**, 191 (2019), arXiv:1805.06596 [hep-ph].
- [54] P. E. Shanahan and W. Detmold, Phys. Rev. Lett. **122**, 072003 (2019), arXiv:1810.07589 [nucl-th].
- [55] K. A. Mamo and I. Zahed, Phys. Rev. D **103**, 094010 (2021), arXiv:2103.03186 [hep-ph].
- [56] X.-H. Cao, F.-K. Guo, Q.-Z. Li, and D.-L. Yao, Nature Commun. **16**, 6979 (2025), arXiv:2411.13398 [hep-ph].
- [57] C. Lorcé and P. Schweitzer, Acta Phys. Polon. B **56**, 3 (2025), arXiv:2501.04622 [hep-ph].
- [58] W. Broniowski and E. Ruiz Arriola, Phys. Rev. D **112**, 054028 (2025), arXiv:2503.09297 [hep-ph].
- [59] F. Hechenberger, K. A. Mamo, and I. Zahed, Phys. Rev. D **113**, 034027 (2026), arXiv:2507.18615 [hep-ph].
- [60] X. Ji and C. Yang, Nucl. Phys. B **1024**, 117342 (2026), arXiv:2508.16727 [hep-ph].
- [61] A. Ali *et al.* (GlueX), Phys. Rev. Lett. **123**, 072001 (2019), arXiv:1905.10811 [nucl-ex].
- [62] B. Duran *et al.*, Nature **615**, 813 (2023), arXiv:2207.05212 [nucl-ex].
- [63] K. A. Mamo and I. Zahed, Phys. Rev. D **101**, 086003 (2020), arXiv:1910.04707 [hep-ph].
- [64] Y. Hatta, A. Rajan, and D.-L. Yang, Phys. Rev. D **100**, 014032 (2019), arXiv:1906.00894 [hep-ph].
- [65] D. E. Kharzeev, Phys. Rev. D **104**, 054015 (2021), arXiv:2102.00110 [hep-ph].
- [66] Y. Guo, X. Ji, and Y. Liu, Phys. Rev. D **103**, 096010 (2021), arXiv:2103.11506 [hep-ph].
- [67] K. A. Mamo and I. Zahed, Phys. Rev. D **104**, 066023 (2021), arXiv:2106.00722 [hep-ph].
- [68] K. A. Mamo and I. Zahed, Phys. Rev. D **106**, 086004 (2022), arXiv:2204.08857 [hep-ph].
- [69] Y. Guo, X. Ji, Y. Liu, and J. Yang, Phys. Rev. D **108**, 034003 (2023), arXiv:2305.06992 [hep-ph].
- [70] O. Ben-Ami, D. Carmi, and M. Smolkin, JHEP **08**, 048, arXiv:1504.00913 [hep-th].
- [71] M. Smolkin and S. N. Solodukhin, Phys. Rev. D **91**, 044008 (2015), arXiv:1406.2512 [hep-th].